Extensive Search for Axion Dark Matter over 1 GHz with CAPP'S Main Axion Experiment

Saebyeok Ahn,[1] JinMyeong Kim,[2,1] Boris I. Ivanov,[1] Ohjoon Kwon,[1] HeeSu Byun,[1] Arjan F. van Loo,[3,4] SeongTae Park,[1] Junu Jeong,[1] Soohyung Lee,[1] Jinsu Kim,[1] Çağlar Kutlu,[1] Andrew K. Yi,[2,1] Yasunobu Nakamura,[3,4] Seonjeong Oh,[1] Danho Ahn,[1] SungJae Bae,[2,1] Hyoungsoon Choi,[2] Jihoon Choi,[1,‖] Yonuk Chong,[5] Woohyun Chung,[1,*] Violeta Gkika,[1] Jihn E. Kim,[6] Younggeun Kim,[1] Byeong Rok Ko,[1,†] Lino Miceli,[1] Doyu Lee,[1,¶] Jiwon Lee,[2,1] Ki Woong Lee,[1] MyeongJae Lee,[1,**] Andrei Matlashov,[1] Pallavi Parashar,[2,1] Taehyeon Seong,[1] Yun Chang Shin,[1] Sergey V. Uchaikin,[1,‡] SungWoo Youn,[1,§] and Yannis K. Semertzidis[1,2]

[1]*Center for Axion and Precision Physics Research, Institute for Basic Science (IBS), Daejeon 34051, Republic of Korea*

[2]*Department of Physics, Korea Advanced Institute of Science and Technology (KAIST), Daejeon 34141, Republic of Korea*

[3]*RIKEN Center for Quantum Computing (RQC), Wako, Saitama 351-0198, Japan*

[4]*Department of Applied Physics, Graduate School of Engineering, The University of Tokyo, Bunkyo-ku, Tokyo 113-8656, Japan*

[5]*SKKU Advancd Institute of Nano Technology (SAINT) and Department of Nano Engineering, Sung Kyun Kwan University (SKKU), Suwon 16419, Republic of Korea*

[6]*Department of Physics, Seoul National University, 1 Gwanak-Ro, Seoul 08826, Republic of Korea*

(Received 21 February 2024; accepted 24 June 2024; published 12 August 2024)

We report an extensive high-sensitivity search for axion dark matter above 1 GHz at the Center for Axion and Precision Physics Research (CAPP). The cavity resonant search, exploiting the coupling between axions and photons, explored the frequency (mass) range of 1.025 GHz (4.24 μeV) to 1.185 GHz (4.91 μeV). We have introduced a number of innovations in this field, demonstrating the practical approach of optimizing all the relevant parameters of axion haloscopes, extending presently available technology. The CAPP 12 T magnet with an aperture of 320 mm made of Nb_3Sn and NbTi superconductors surrounding a 37 l ultralight-weight copper cavity is expected to convert Dine-Fischler-Srednicki-Zhitnitsky axions into approximately 10^2 microwave photons per second. A powerful dilution refrigerator, capable of keeping the core system below 40 mK, combined with quantum-noise-limited readout electronics, achieved a total system noise of about 200 mK or below, which corresponds to a background of roughly 4×10^3 photons per second within the axion bandwidth. The combination of all those improvements provides unprecedented search performance, imposing the most stringent exclusion limits on axion-photon coupling in this frequency range to date. These results also suggest an experimental capability suitable for highly sensitive searches for axion dark matter above 1 GHz.

DOI: 10.1103/PhysRevX.14.031023

Subject Areas: Astrophysics, Nuclear Physics, Particles and Fields

I. INTRODUCTION

Dark matter, which is evident in many astronomical observations, is generally accepted to be one of the major substances in our Universe, making up approximately 85% of matter and strongly influencing the formation and evolution of galaxies [1,2]. However, the mysterious hypothetical substance has eluded decades of dedicated searches. It remains invisible and its identity unknown. The possible candidates for dark matter include individual heavy particles, such as weakly interacting massive particles [3,4], coherently oscillating waves such as axions (in generic, axionlike particles) [5,6], or astronomical objects such as primordial black holes [7,8]. Among these, axions are theoretically promising particles that were originally proposed to solve a fundamental problem in strong

*Contact author: gnuhcw@ibs.re.kr
†Contact author: brko@ibs.re.kr
‡Contact author: uchaikin@ibs.re.kr
§Contact author:swyoun@ibs.re.kr
‖Present address: Korea Astronomy and Space Science Institute, Daejeon 34055, Republic of Korea.
¶Present address: Samsung Electronics, Gyeonggi-do 16677, Republic of Korea.
**Present address: Department of Physics, Sungkyunkwan University, Suwon 16419, Republic of Korea.

interactions, known as the strong-*CP* problem. The charge-parity (*CP*) symmetry that is expected to be violated according to quantum chromodynamics (QCD) of the standard model (SM) appears to be conserved in nature, as indicated by the absence of an electric dipole moment for the neutron [9] and proton [10]. An elegant solution to this naturalness problem is the Peccei-Quinn (PQ) mechanism, where the *CP*-violating term in the QCD Lagrangian, parametrized by $\bar{\theta}$, is promoted to a scalar field by introducing a new U(1) global symmetry as a minimal extension of the SM [11]. The symmetry becomes spontaneously broken at some energy scale, dynamically relaxing the $\bar{\theta}$ parameter to zero, thus resolving the strong-*CP* problem. The Goldstone boson associated with the spontaneous symmetry breaking is the axion [12,13]. The mass and coupling (strength of axion-photon interaction) are inversely proportional to the symmetry breaking scale f_a, also known as the decay constant. Since searches for the standard axion at $f_a \sim v_{\mathrm{EW}}$ (electroweak scale) have yielded null results, attention has shifted to detecting "invisible" axions with very large f_a, i.e., with very small mass and very weak coupling to ordinary matter. Although these QCD axions are specifically motivated to resolve the *CP* problem in QCD, there is a more general type of particles, called axionlike particles, which are not necessarily related to QCD but arise in various extensions of the SM of particle physics.

The unique properties of the axion turn out to provide a suitable explanation for the missing matter of the Universe. Depending on the production and evolution of the cosmic axion field, there are two possible scenarios for axion cosmology. In the preinflationary scenario, where cosmic inflation selects a particular region of the Universe free of topological defects, often referred to as a "patch," the PQ symmetry breaking results in a homogeneous initial misalignment value of the axion field throughout the observable Universe and determines the axion relic (present) density with a mass within a wide range as low as 1 peV/c^2, where c is the speed of light, accounting for the present abundance of dark matter [14,15]. Alternatively, the postinflationary axion field embraces many patches and thus takes on multiple initial values, resulting in topological defects that additionally contribute to axion production. Using a spatially averaged initial misalignment value, early studies imposed a cosmological constraint on the decay constant $f_a \lesssim 10^{12}$ GeV, which set a lower bound of $\gtrsim$1 μeV on the mass [16–18]. Recent advancements in QCD lattice calculations and simulations have provided predictions for the axion mass within a relatively narrow range, typically from $\mathcal{O}(10^1)$ to $\mathcal{O}(10^2)$ μeV [19–21].

At present, dark-matter axions are assumed to be in a virialized state (a sort of thermalization process without energy loss from the total system) with their velocity following the Maxwell-Boltzmann distribution. This results in a dispersion of $\sim 10^{-3}c$, which in turn yields an average quality factor of 1.0×10^6 for an observer on Earth [22].

Although feeble, the QCD axion can interact with SM particles through anomalous couplings to gluons. Depending on the type of particles contributing to the anomalous loop, there are two general classes of invisible axion models: Kim-Shifman-Vainshtein-Zakharov (KSVZ) with a newly introduced heavy quark carrying the PQ charge [23,24] and Dine-Fischler-Srednicki-Zhitnitsky (DFSZ) with ordinary quarks and leptons carrying the charge [25,26]. The electromagnetic interaction has been widely accepted for practical searches, since it mediates axion-photon coupling, providing an experimental signature, i.e., photons, which can be detected with existing well-developed detection technologies.

The detection principle, first suggested by Sikivie [27], relies on the macroscopic version of the (inverse) Primakoff effect, where a classical magnetic field serves as a sea of virtual photons with which axions interact and convert into real photons. The photon frequency corresponds to the total energy of the detected axion. There are several types of search strategies depending on the source of the axion. These include (i) haloscope searches for dark-matter axions in the galactic halo (CAPP [28–32], ADMX [33–35], HAYSTAC [36–38], QUAX [39–41], ORGAN [42,43], MADMAX [44–46], DM Radio [47], CAST-CAPP [48], FLASH [49], etc.), (ii) helioscopes pointing at the Sun to look for solar axions (CAST [50] and IAXO [51]), and (iii) light-shining-through-the-wall schemes, which are configured to generate and detect axions in the lab (OSQAR [52] and ALPS (II) [53,54]). Among these, the cavity haloscope method provides the most sensitive approach, particularly in the microwave region under the assumption that axions contribute significantly to the local density of dark matter.

A cavity haloscope consists of a microwave resonator immersed in a strong magnetic field where axions induce photons that couple with one of the cavity resonant modes, e.g., the TM_{010} mode for a cylindrical geometry. The expected power of the axion-photon conversion (assuming no coupling to external circuit) is given by [55]

$$P_{a\gamma\gamma} = 8.7 \times 10^{-23}\ \mathrm{W} \left(\frac{g_\gamma}{0.36}\right)^2 \left(\frac{\rho_a}{0.45\ \mathrm{GeV/cm^3}}\right) \times \left(\frac{\nu_a}{1.1\ \mathrm{GHz}}\right) \left(\frac{\langle \mathbf{B}_e^2 \rangle}{(10.3\ \mathrm{T})^2}\right) \left(\frac{V_c}{37\ \mathrm{l}}\right) \left(\frac{G}{0.6}\right) \times \left(\frac{Q_a \cdot Q_c}{Q_a + Q_c} \frac{10^6 + 10^5}{10^6 \times 10^5}\right), \quad (1)$$

where g_γ is the model-dependent coupling coefficient that determines the axion-photon coupling given by the relation of $g_{a\gamma\gamma} = (\alpha/\pi)(g_\gamma/f_a)$, where α is the fine structure constant. For the KSVZ and DFSZ models, the values of g_γ are -0.97 and 0.36, respectively. ρ_a is the axion density

in the local dark-matter halo, ν_a is the axion Compton frequency, $\langle \mathbf{B}_e \rangle$ denotes the average of the square of the externally applied magnetic field within the cavity volume V_c, while Q_a and Q_c correspond to the quality factors of the dark-matter axion and the (unloaded) cavity, respectively. G is the form factor associated with the resonant mode, providing a measure of how well the external magnetic field is matched with the electric field associated with the relevant cavity mode ($\mathbf{E}_c$):

$$G = \frac{|\int \mathbf{E}_c \cdot \mathbf{B}_e dV_c|^2}{\int \varepsilon_r |\mathbf{E}_c|^2 dV_c \times \int |\mathbf{B}_e|^2 dV_c}, \tag{2}$$

where ε_r is the dielectric constant inside the cavity. Only a fraction of the conversion power is detected as a signal by a radio-frequency (rf) antenna coupled to the cavity with a coupling coefficient β. The signal power $P_{\rm sig}$ is expressed as $P_{\rm sig} = (\beta/1+\beta)P_{a\gamma\gamma}$ with Q_c now replaced by $Q_l = Q_c/(1+\beta)$, known as the loaded quality factor. Assuming that local dark matter is composed solely of DFSZ axions, a cavity haloscope with the experimental parameters used in Eq. (1) would expect about 120 photons/s to be converted in the cavity and about 30 photons/s to be picked up by a critically coupled ($\beta = 1$) receiver antenna.

A measure of experimental sensitivity is given by the signal-to-noise ratio (SNR),

$$\mathrm{SNR} \equiv \frac{P_{\rm sig}}{\delta P_{\rm syst}} = \frac{P_{\rm sig}}{k_B T_{\rm syst}} \sqrt{\frac{\Delta t}{\Delta \nu}}, \tag{3}$$

where $\delta P_{\rm syst} (= P_{\rm syst}/\sqrt{\Delta\nu \Delta t})$ denotes fluctuations in system noise power over a bandwidth $\Delta\nu$ during an integration time Δt, and $P_{\rm syst} (= k_B T_{\rm syst} \Delta\nu)$ describes the Johnson-Nyquist noise with the Boltzmann constant k_B and the system noise temperature $T_{\rm syst}$. Since the axion mass is unknown *a priori* and the allowed mass range is vast, a fast scanning speed with a given sensitivity becomes the figure of merit for the experimental design. The relevant quantity is obtained by inserting Eq. (1) into Eq. (3) as

$$\frac{d\nu}{dt} = 1.2 \frac{\mathrm{GHz}}{\mathrm{yr}} \left(\frac{\eta}{0.6}\right) \left(\frac{5}{\mathrm{SNR}}\right)^2 \left(\frac{0.2\,\mathrm{K}}{T_{\rm syst}}\right)^2 \times \left(\frac{P_{\rm sig}}{2.1\times 10^{-23}\,\mathrm{W}}\right)^2 \left(\frac{Q_a}{10^6}\right) \left(\frac{Q_a \cdot Q_l}{Q_a + Q_l} \frac{10^6 + 10^5/3}{10^6 \times 10^5/3}\right), \tag{4}$$

where η is the data acquisition (DAQ) efficiency, reflecting the temporal duty cycle, while SNR is the SNR value targeted by an experiment. Equation (4) assumes an optimal coupling strength $\beta = 2$ that maximizes the scanning speed [55]. Major research and development efforts have been made to increase the search rate by maximizing the figure of merit (FOM $\equiv B_e^4 V^2 G^2 Q_c / T_{\rm syst}^2$), the metric that defines the strength of the experiment for a given frequency.

The Center for Axion and Precision Physics Research (CAPP) of the Institute for Basic Science (IBS) was established in October 2013 at the Korea Advanced Institute of Science and Technology (KAIST) in Daejeon, Republic of Korea. IBS-CAPP's main focus has been cavity haloscope searches utilizing multiple experimental setups designed for different mass regions. Among them, CAPP-MAX (main axion experiment), formerly known as CAPP-12 TB, is the most sensitive (flagship) experiment at CAPP, taking advantage of available cutting-edge technologies learned from smaller experiments running in parallel. The main components of the system include a superconducting solenoid with a center field of 12 T, based on a Nb_3Sn superconducting magnet (inner) and a regular NbTi superconducting magnet (outer), built by Oxford Instruments [56]. A cryogenic dilution refrigerator (DR) with a measured cooling power of 1 mW at 90 mK is capable of reaching a base temperature of 5.6 mK. The detector comprises a 37 l lightweight copper cavity connected to a readout chain consisting of flux-driven Josephson parametric amplifiers (JPAs) [57], followed by a series of linear semiconductor amplifiers. This experiment has recently reported a search using unprecedented sensitivity to probe DFSZ axion physics above 1 GHz [32,58] of about 20 MHz. In this paper, we report new results from an extended search for invisible axion dark matter with CAPP-MAX, the first search at or near DFSZ sensitivity over a large frequency range of more than 100 MHz above 1 GHz.

The remainder of this paper is organized as follows. In Sec. II, we introduce the major experimental equipment including the 12 T superconducting magnet and the wet-type cryogenic dilution refrigerator system. Their manufacturing specifications and the actual measurements of the relevant parameters such as magnetic field and base temperature are provided. Section III describes the detection system consisting of the microwave cavity and readout electronics, featuring quantum-noise-limited amplifiers (QNLAs) in the first stage of the chain. The characteristics and quality of the individual components are presented in sufficient detail, with particular focus on noise calibration and cavity performance. Section IV is dedicated to the automated data acquisition and monitoring system, specifically designed for continuous data flow and high-efficiency real-time monitoring of the entire system. Section V presents the analysis procedure and the results. The analysis follows the standard procedure commonly adopted in the community and is similar to the analysis reported in our previous searches [28–32,58]. Finally, we highlight the importance of the experimental results and provide a perspective for our near-future work in Sec. VI.

II. MAJOR EQUIPMENT

A. Magnet

The FOM in axion haloscope searches is dominated by the strength and volume of the magnet, making it the key factor in CAPP-MAX. Our superconducting magnet, classified as "wet," requires direct contact with liquid helium (LHe) to maintain the coils in a superconducting state. It has three main characteristics.

(1) The cylindrical magnet used in our experiment, manufactured by Oxford Instruments [56], can operate at a central magnetic field of 12 T when cooled to a temperature of 4.2 K using LHe. In Fig. 1, the magnetic-field map in the cavity region is shown in the plot on the left. The total energy content of the magnet, when fully energized to 12 T, is 5.562 MJ.

(2) The solenoidal magnet used in CAPP-MAX features a cold bore diameter of 320 mm. This magnet consists of two distinct low-temperature superconductors: Nb_3Sn for the inner coil and NbTi for the outer one. These coils are nested together to create a concentric solenoid. It is worth noting that Nb_3Sn coils can withstand magnetic fields well exceeding 12 T, albeit at a higher cost, while NbTi coils, although more economical, have a lower tolerance, reaching their limit around 9 T. The inner coil has a length of 560 mm, while the outer has a length of 640 mm. Taking into account the dimensions of the coil and the radiation shields of the dilution refrigerator insert (see Sec. III), the experiment can accommodate a cylindrical cavity with a volume of 37 l inside the solenoidal magnet's bore. The average of the square of the externally applied magnetic field along the magnet axis over this volume measures 10.55 T.

(3) The field cancellation region is located 750 mm above the center of the magnet, and has both diameter and length dimensions of 100 mm in cylindrical coordinates. The cancellation coil is connected in series with the main solenoid, sharing the same power supply and superconducting short circuit. Within this region, the generated magnetic fields are weaker than 10^{-2} T, as illustrated on the right of Fig. 1. The presence of this cancellation region is of utmost importance to ensure the proper operation of the JPAs, which serve as the initial-stage rf amplifier, as well as for the required microwave circulators and other rf components in the setup.

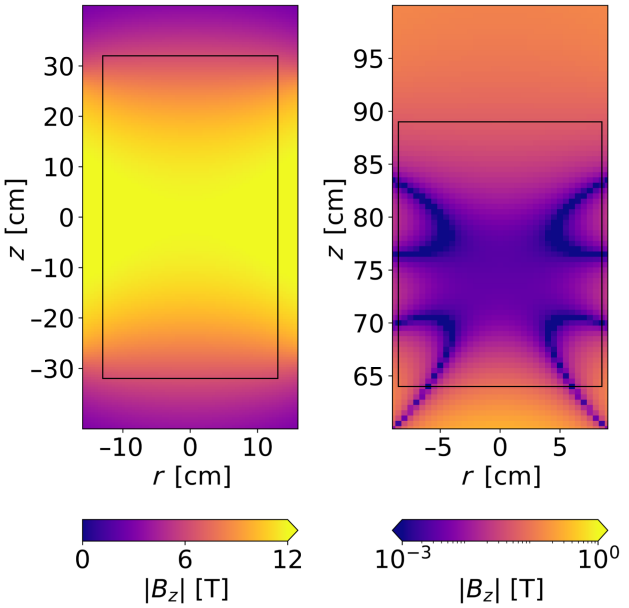

FIG. 1. Simulation of the magnetic-field distributions in the cavity region (left) and cancellation region (right). The coordinates z and r refer to the longitudinal and radial axes of the solenoid, correspondingly. The black outline on the left corresponds to the location of the cavity, while on the right it corresponds to the location of the JPA assembly. The magnet dimensions are given in the text.

The combination of three characteristics discussed above are unparalleled worldwide, allowing us to conduct axion dark-matter searches with increased sensitivity [32,58]. These distinctive features not only enabled our current research but also pave the way for continued investigations into axion dark matter at higher frequencies.

The magnet can be safely ramped up at a rate of 0.13 T/ min without any load inside the magnet bore. In addition, the magnet system also incorporates a crucial feature known as persistent-mode operation, which allows it to operate without the need of an external power supply once it has been ramped up.

This persistent-mode operation significantly reduces the evaporation rate of LHe to 30 l/day, compared to 40 l/day during driven-mode operation. The decay rate of persistent mode operation is approximately 30 ppm/day, which has no practical impact on a typical axion-haloscope search schedule.

The magnet system underwent a quench test to evaluate its response before delivery by Oxford Instruments [56,59]. It has been successfully installed inside a vapor shield cryostat, with a height of approximately 3.3 m. The cryostat provides a useful volume of 478 l for containing the LHe. The magnet system was delivered to the CAPP experimental hall in March 2020. However, due to the impact of the COVID-19 pandemic, the commissioning run was delayed until August of the same year and finally completed in December 2020. The magnet was powered up in spring 2021 and has been maintained at a cold temperature, with only one instance of raising its temperature above 100 K up to summer 2023.

Our magnet weighs approximately 1200 kg, and it is most convenient to keep it on a low vibration platform (LVP) of our experimental hall during operation and during

the period between experiments. This necessity requires us to move the DR up and down during the installation and warming-up procedures. The LVP helps reduce the vibration effects resulting from the mechanical motion of vacuum and cryogenic equipment on both the cavity and the signal output. This reduction in vibration amplitude ranges from a factor of 30 at 10 Hz to 3000 at 100 Hz, as measured after installation by the manufacturer.

B. Cryogenics

One of the critical factors in Eq. (3) is the system noise temperature, which is composed of various components, including the cavity, the initial amplifier stages, passive rf components, cable and connector losses, among others. To minimize the impact of these effects, it is essential to reduce their physical temperature. Furthermore, certain components, such as QNLAs, operate only under cryogenic conditions, and their added noise depends on their physical temperatures. High-electron-mobility-transistor (HEMT) amplifiers, while functional over a wide temperature range, exhibit their best noise properties below 10 K [60,61]. Therefore, having cryogenic equipment capable of cooling these crucial components in the readout circuit is essential to achieve the best performance of the system.

The determination of how low we need to cool our critical components can be derived from our target frequency range, which, for CAPP-MAX at this stage, falls between 1 and 2 GHz. According to the standard quantum limit, the noise temperature ($T_{\mathrm{SQL}} = \hbar\omega/k_B$) for a frequency of 1 GHz is 48 mK, one component of which is the added amplifier noise of 24 mK for 1 GHz ($T_{\mathrm{add,min}} = \hbar\omega/2k_B$). This provides us with guidance on the cooling temperatures required for our components to achieve optimal performance. Temperatures below 30 mK can be achieved with a standard dilution refrigerator.

Another part of our system that requires cryogenic temperatures is the superconducting magnet, manufactured by Oxford Instruments and featuring a complex design (see Sec. II A). During a warm-up phase of the magnet to 100 K, in order to remove solidified nitrogen and oxygen from the main Dewar, the outer vacuum chamber (OVC) was pumped to improve the isolation and remove any penetrating gas. This process improved vacuum isolation and reduced the helium gas pressure in the main Dewar by a factor of 6.

We utilize a Leiden Cryogenics DRS1000M [62] dilution refrigerator, which offers a nominal cooling power of approximately 1.3 mW at a temperature of 120 mK (marked as Dilution refrigerator in Fig. 2). The DR is equipped with three clear 25-mm-diameter tubes extending from the top of the DR down to the 4 K stage, which is used for wiring purposes. Three 24-pin Fischer connectors [63] facilitate connections to the mixing chamber (MXC), while one of the connectors is used for wiring to the 4 K plate. The wiring is constructed of phosphor-bronze twisted pairs. Two differential lines are used to control the piezoactuators, and they are made of copper wire that runs from the room-temperature (RT) flange down to the 4 K plate. From the 4 K plate down to the MXC, four and five differential pairs made out of NbTi wires are connected in parallel to enable the supply of high-current pulses, with amplitudes reaching a few amperes, to the piezoactuators.

All rf connections that run from the RT flange to the 4 K plate are constructed using 0.034-in.-diameter CuNi cables. One of these cables is kept as spare and kept terminated inside the DR. The next four cables that connect the system inputs are made of 0.047-in.-diameter BeCu cables, while the output cable is constructed from superconducting 0.034-in.-diameter NbTi cables. All interconnections between cables are made using gold-plated Sub Miniature version A (SMA) connectors and bulkheads are constructed of brass and BeCu.

The DR is equipped with five standard temperature sensors from Leiden Cryogenics, which are used to monitor the temperature and control it through a proportional-integral-differential (PID) controller. We used an additional 10 channels to accurately measure the following temperatures: 4 K plate, two HEMT amplifiers, two microwave circulators thermally anchored to the cold plate, the top and bottom of the cavity, and the extension of the mixing chamber. One of the thermometers was attached to the piezorotator within run 4 and later on it was placed at the cold plate within run 5.

The inner vacuum chamber (IVC) shield maintains a temperature at the level of LHe, while inside, there is an immersed gold-plated radiation shield with a temperature ranging from approximately 550 to 800 mK during the refrigerator operation. Because of space constraints, we have opted not to use the radiation shield that is typically thermally connected to the refrigerator's cold plate. This is one of the reasons why the base temperature is higher than the base temperature specified in the manual.

The DR is immersed in an LHe cryostat, which also houses a superconducting magnet. The IVC is filled with helium exchange gas, which aids in precooling the DR insert to LHe temperature. Before immersing the DR, the 1 K pot needs to be pressurized, typically to a pressure of around 1.3 bar. This pressurization is essential to prevent nonpurified helium gas, which may include slight nitrogen contamination, from entering these capillaries connecting the 4 K pot to the cryostat. If helium gas mixed with nitrogen were to penetrate these capillaries, it could lead to the antisublimation of nitrogen on the capillary walls. This, in turn, could block the capillaries, rendering the operation of the 1 K pot ineffective or even impossible.

Once the DR insert reaches approximately liquid-helium temperature, we initiate the process of pumping out the exchange gas from the IVC using dry rotary and

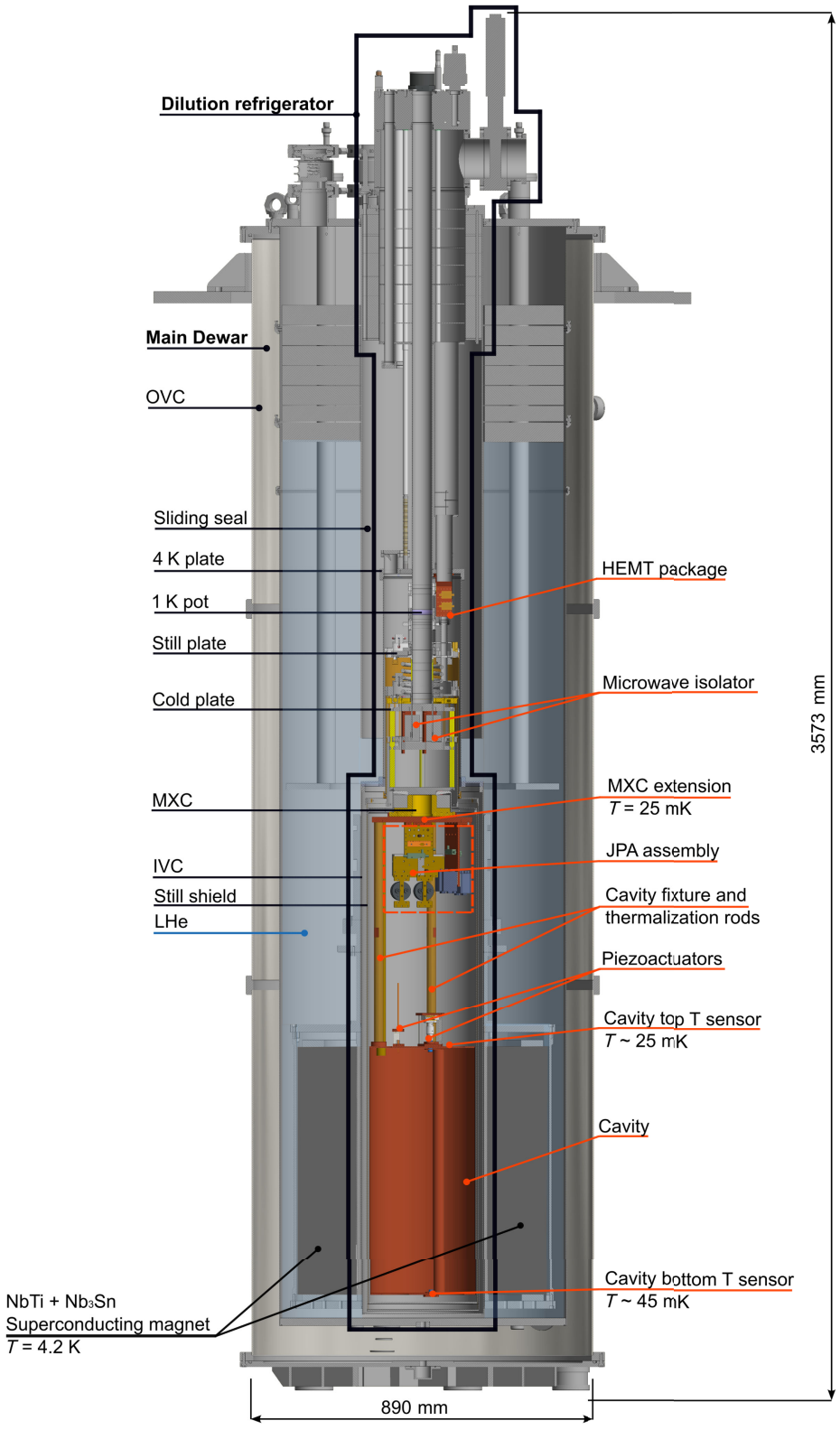

FIG. 2. Comprehensive view of the detector setup within the cryostat. It includes a cross-sectional view of the main Dewar containing LHe and the inserted dilution refrigerator (outlined in black). The HEMT package is located on the 4 K plate, while the microwave isolator is located on the cold plate. The cavity and MXC assembly are affixed to the gold-plated copper extension of the mixing chamber via four gold-plated copper thermalization rods. The Still radiation shield is linked to the Still extension. The cavity has two temperature sensors to monitor top and bottom temperatures and two piezoactuators to adjust the cavity resonance and coupling coefficient.

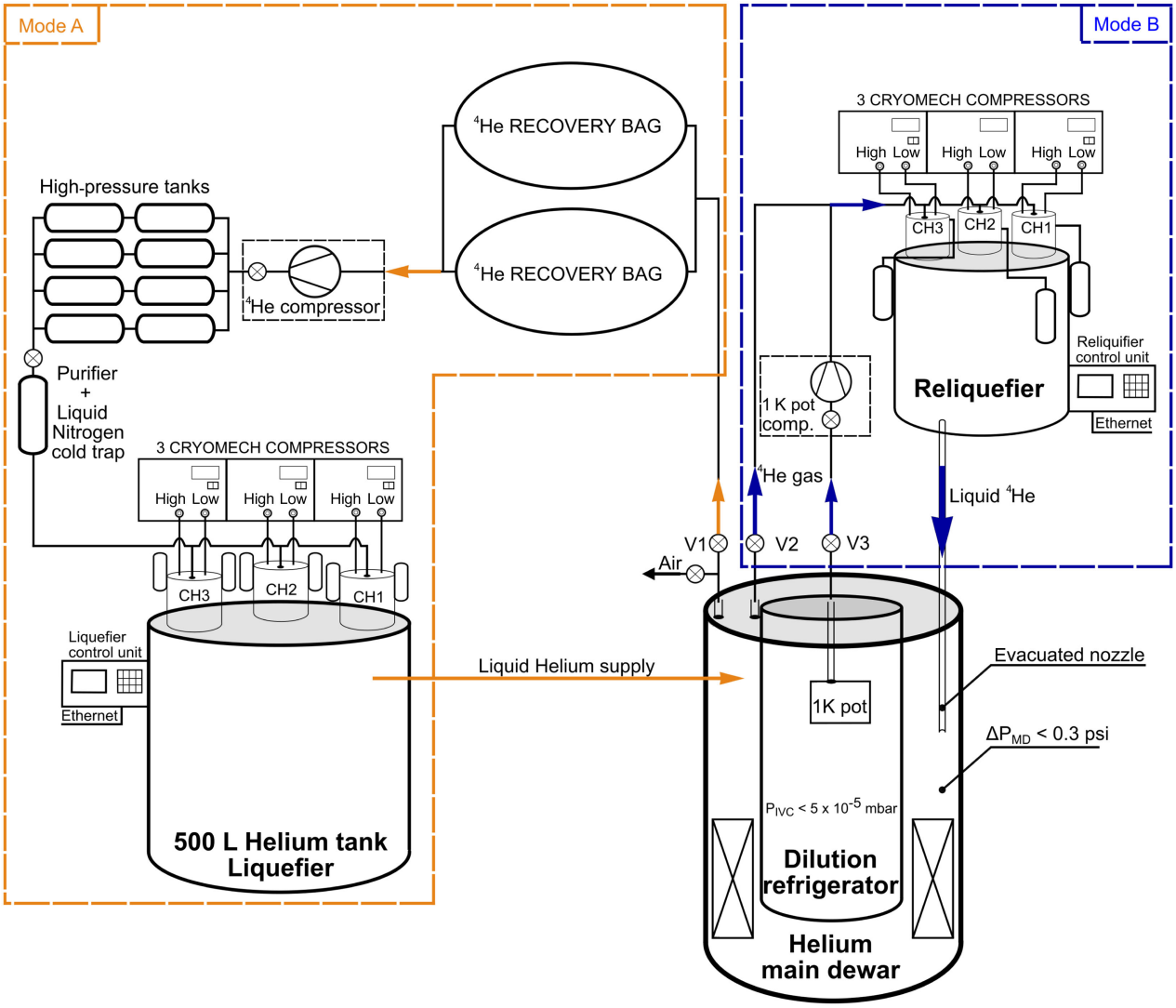

FIG. 3. Schematic view of the helium gas recovery system operating in two modes shown with orange and blue dashed outlines. Mode A: during dilution refrigerator (DR) insertion and during the main Dewar maintenance. Mode B: during data taking. In the first configuration mode, the main recovery line is followed by the manual valve (V1), the two He gas recovery bags and the Cryomech He compressor (model HRCP), the eight high-pressure tanks, the purifier (model HRSMP-Purifier), the three cold heads (CH1–CH3) (model PT415) charged by the Cryomech He compressors (model CP1110) placed on the top of the 500 l nonmagnetic He liquefier (model LHeP60), and the liquid-cryogen level monitor (model LM-510) with PID control. In the second mode, the He closed-cycle operation is used. The main Dewar is followed by the manual valve (V2), the reliquefier (RL) (model HeRL60), the three cold heads (CH1–CH3) (model PT420-RM), charged by the 3 Cryomech compressors (model CPA1114). The pressure and the temperature control unit with PID from Stanford research systems (model CTC100) is used. The output of the reliquefier is followed by the evacuated-jacket metal nozzle. The 1 K pot of the dilution refrigerator is followed by the manual valve (V3), by the Cryomech 1 K pot compressor (model PHRS1E350006), and is connected to the input of the RL. In mode B, we keep the main Dewar pressure over 1 atm, with ΔP_{MD} lower than 0.3 psi.

turbomolecular drag pumps, reducing the pressure below 5×10^{-5} mbar. This process typically takes about 18 hours to complete and requires running the sorption pump heater. The primary cooling process takes place predominantly within the 1 K pot. LHe is delivered from the main Dewar through two tubes connected to the 4 K plate. From there, it flows through thin capillaries, filling the 1 K pot with LHe. To facilitate cooling, the 1 K pot is pumped using an external compressor, shown as "1 K pot comp." in Fig. 3. As pumping progresses, the temperature of the 1 K pot drops to the range of 1.4–1.8 K, and it also precools the insert part of the DR.

Once the 1 K pot is sufficiently cold, the ^{3}He-^{4}He mixture can be introduced into the fridge by the condensing process. When the mixture is filled into the MXC, circulation can begin. This circulation causes the still and mixing chamber to cool to below 1 K. Once the mixing chamber has reached its base temperature (for fully

loaded DR it is currently about 25 mK), the Still heater can be activated, typically requiring a couple of milliwatt of power. In this way we are able to control the flow rate of the mixture. Generally, with this level of heating power, the pressure in the Still line stabilizes at around 8.2×10^{-2} mbar.

The cooling power and time of each stage in a dilution refrigerator depend on several factors, including the design of the refrigerator, the heat load imposed on it, and the heat capacitance of the components integrated into the custom system. Achieving a good thermal connection between components is a crucial practical consideration. When two surfaces touch, the actual contact occurs only at the points where there are protrusions or asperities. To ensure effective connection, it is necessary to increase the contact area by plastic deformation by applying pressure during the connection process. Additionally, to compensate for thermal expansion and contraction in linear dimensions when using threaded links, spring washers should be employed. To eliminate the effect of metal oxide on the surface during thermalization, copper parts are gold plated.

To increase the surface area of contact between dielectrics or between dielectrics and metals, we apply Apiezon N grease [64] between them. In general, we aim to minimize the use of dielectric components or reduce their size on the millikelvin stages to expedite the cooling process and limit their impact.

The rf cables were thermally connected to the bulkheads on the 4 K stage and the MXC. They were also thermally linked to the heat exchangers of the DR in between. We used superconducting cables at temperatures below 4 K.

The main evaporation of the He gas comes from the main Dewar and the 1 K pot of the DR. In order to avoid any helium losses during the maintenance of the main Dewar, the insertion of the DR, and the data taking process, we use He recovery lines (controlled by V1, V2, V3; see Fig. 3).

The initial He recovery line operates during the insertion of the DR into the main Dewar or while warming up or cleaning the main Dewar of contamination (mode A in Fig. 3). For this operation, we employ a LHeP60 helium liquefier plant [65], with the ability to liquefy up to 60 l helium per day and equipped with a storage capacity of 60 l of helium gas in gas tanks.

This line consists of two He recovery bags, a helium compressor, high-pressure tanks, two purifiers for water absorption, a liquid-nitrogen cold trap, and a 500 l helium tank (referred to as Liquefier in Fig. 3). Three cold heads, marked CH1–CH3 in Fig. 3, run the condensing process of the incoming He gas flow. The PID system, based on the cryogenic level monitor, controls the temperatures of the cold heads and the pressure within the liquefier's Dewar.

After the He liquefaction, the transfer of liquid He to the main Dewar is accomplished by directly connecting the main Dewar and the liquefier Dewar using an evacuated siphon. The liquefier Dewar is constructed from nonmagnetic metals, allowing its placement in close proximity to the main Dewar, even within the high magnetic-field area. The Cryomech He compressor is complemented by closed-cycle distilled water chillers, positioned outside the laboratory building for better cooling efficiency.

The second He recovery line, identified in the mode B in Fig. 3, operates in a closed He loop and does not require a high-volume He reservoir. The He gas evaporates from both the He main Dewar, through valve 2, and from the 1 K pot, through valve 3, shown with arrows in Fig. 3 to the liquefier tank and condenses at the three cold heads.

The liquid helium is returned to the main Dewar via a vacuum thermoisolated nozzle. The vertical position of the reliquefier (RL) HeRL60 [66] is adjustable. Varying the height of the RL maintains high operational efficiency since it keeps the end of the nozzle slightly above the liquid helium level. The incorporation of an evacuated jacket around the metal nozzle has effectively reduced internal helium evaporation from the main Dewar, resulting in a substantial decrease in the main Dewar pressure from 2.4 psi to nearly 0 psi. In this way, we are able to set the PID system to support 0.3 psi of the input pressure using internal heaters inside of the RL. During the data taking, the liquid He flows continuously, closing the loop between the RL and the main Dewar.

III. DETECTION SYSTEM

A. Microwave cavity

The axion haloscope employs a tunable cavity with a high quality factor, placed in a strong magnetic field, to detect signals generated when the axion frequency falls within the cavity resonance. As seen in Eq. (1), the larger the magnetic field and cavity volume, the more of the axion dark-matter field is converted into microwave photons. A higher quality factor results in converted microwave photons surviving inside the cavity for longer periods, amplifying the signal.

The CAPP-MAX relies on a powerful 12 T magnetic field generated within a large 320 mm bore. This requires the design of a large cavity that allows high B^2V. To address this, CAPP designed an ultralight cavity (ULC) that weighs less than 5 kg including the tuning rod and occupies a volume of 37 l, while maintaining a Q factor of approximately 10^5. This enables axion searches within the range 1.02–1.185 GHz.

The size of the cavity for the CAPP-MAX is influenced by the bore size of the magnet and the dimensions of its various internal radiation shields. The innermost 50 mK shield is positioned within the Still radiation shield, with an inner diameter of 281 mm. Based on this fact, the outer diameter of the cavity was determined to be 274 mm. In the described axion experiments, the 50 mK shield was not

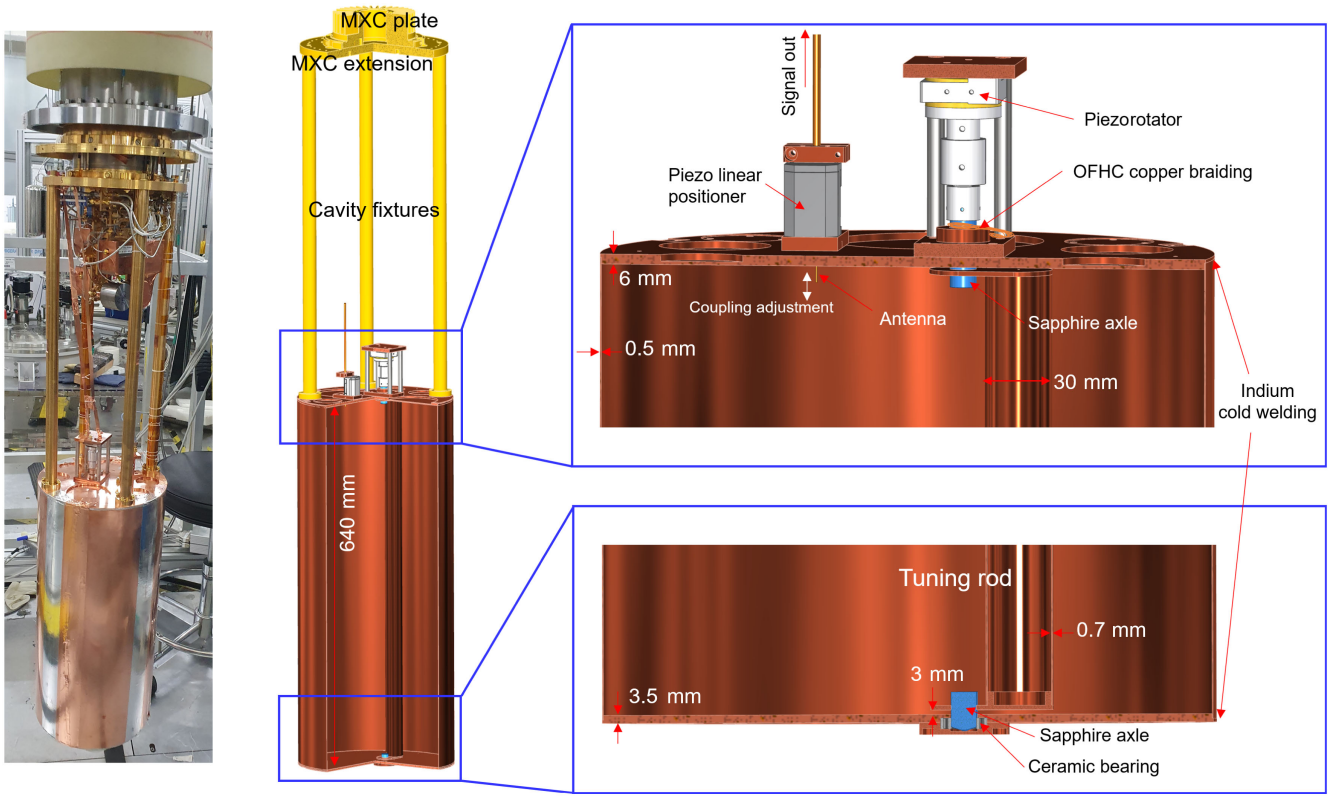

FIG. 4. Photograph of the ULC (left), a three-dimensional cross-sectional view of the mechanical design (middle), and an enlarged view of the top and bottom (right). The four cavity fixtures and thermalization rods made of gold-plated copper thermally anchor the cavity which is affixed to the MXC extension. The piezolinear positioner adjusts the antenna coupling between the readout chain and the cavity. The piezorotator steers the copper tuning rod with the sapphire axle, which is thermalized via OFHC copper braiding. Indium cold welding connects the cavity top and bottom to the side walls.

utilized. Without the 50 mK shield, the additional heat load generated from the Still shield, when calculated according to the Stefan-Boltzmann law, is negligible, amounting to less than 0.1 μW. This decision has shortened the system setup time and provided additional space, enabling the use of larger cavities in subsequent experiments, thereby enhancing sensitivity.

To minimize space loss due to the thickness of the cavity walls and to reduce its weight, thin metal sheets were rolled to create the cavity's side walls. Oxygen-free high-thermal-conductivity (OFHC) copper, known for its high thermal and electrical conductivity, was used as the material of choice, allowing for a high Q factor while facilitating effective cooling. Figure 4 depicts the structure of the first CAPP-MAX cavity. The top and bottom plates of the cavity are 6 and 3.5 mm thick, respectively. The height of the cavity is 640 mm with the thickness of its side walls 0.5 mm. Excluding the tuning rod, the ULC weighs only about 4 kg.

To adjust the resonance frequency of the cavity, we rotated the position of a 436 g empty cylinder with a diameter of 30 mm, a height of 636 mm, a thickness of 0.7 mm within the cavity, and the rotation axis located 25 mm away from the center of the cavity. The total weight of the tuning rod mechanism, including the sapphire axles is 460 g. This rotation had a 50 mm diameter that can be used to tune the TM_{010}-like mode resonance frequency in the range 1.02–1.185 GHz. Simulations show [67,68] that the tuning rod's relatively small size compared to the cavity diameter and its restricted movement within 50 mm from the cavity center help mitigate the mode localization often observed when using a metal tuning rod in cavities [38]. We attached a sapphire axle to the center of rotation of the tuning rod, allowing precise tuning with a resolution of less than 1 millidegree using the piezorotator from Attocube Systems AG [69]. This setup allowed for a tuning resolution of less than 1 kHz. Additionally, the alignment of the upper and lower sapphire axles was adjusted within a 1 mm margin of error to keep the maximum tilting angle of the tuning rod below 0.2 deg, ensuring that the form factor is maintained to within about 1%. Studies, using the bead-pull method [70], in which the electric field strength is probed as a function of position within the cavity, were performed, ensuring that the mechanical tolerances are acceptable. The bead-pull method was performed with a smaller cavity (<2 l), and the results were stable and consistent with the simulations for the TM_{010}-like mode despite a relatively large tolerance ($\sim$0.5 mm).

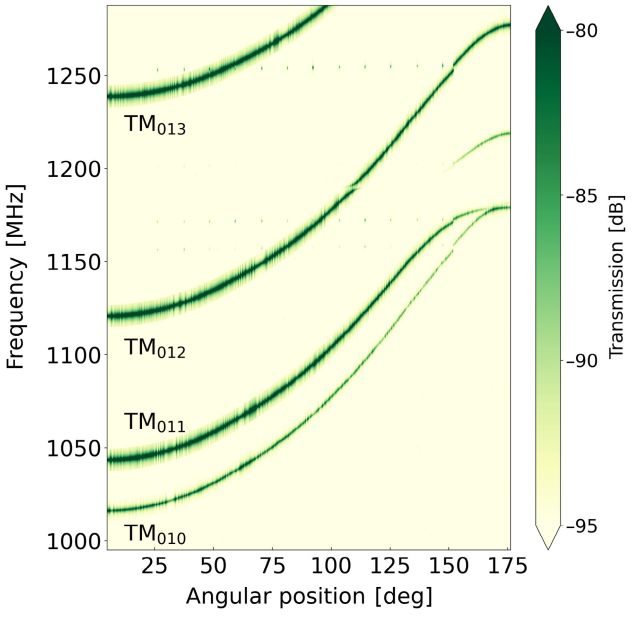

(a)

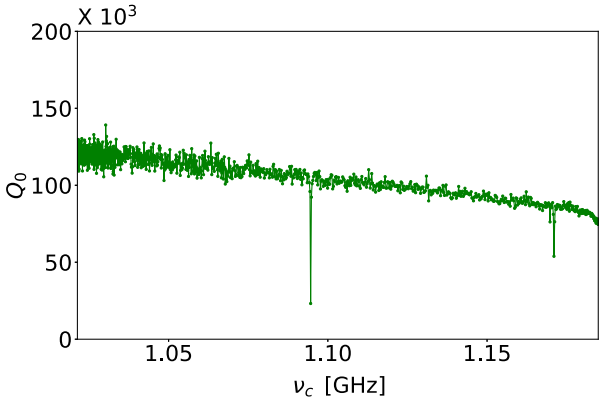

(b)

FIG. 5. Cavity parameters obtained at 4.2 K. (a) Mode map: resonant frequency versus angular position of the tuning rod, with 180 deg corresponding to the center of the cavity. The intensity of the lines corresponds to the forward transmission coefficient (S21) in logarithmic scale. The individual modes are identified from simulation. (b) Unloaded quality factor as a function of frequency. The two vertical dips correspond to mode crossings.

Transmission scattering parameters were measured using a vector network analyzer (VNA) to create a mode map and the Q factor versus the resonance frequency of the cavity for the 1–1.2 GHz frequency range, as shown in Fig. 5. The mint-colored line at the bottom of the mode map represents the resonance frequency range of the TM_{010} mode. Although minor mode crossings occurred at some frequencies throughout the tuning range, there were no significant mode mixings, consistent with the initial design. The unloaded cavity Q factor was greater than 1.2×10^5 when the tuning rod was farthest from the center (50 mm) and remained at 0.9×10^5 when positioned at the center, maintaining over 10^5 throughout most of the tunable frequency range.

Effective thermal management is essential to minimize the physical noise from the cavity and the tuning rod. The key steps involve optimizing thermal conductivity, reducing the number of thermal interfaces, and enhancing efficiency at inevitable interfaces [71].

Initially, we secured four OFHC copper rods with gold plating to the upper part of the cavity using bolts. This approach facilitated efficient thermalization. The interfaces between the upper and lower cavity sections were bonded through indium cold welding. Furthermore, OFHC copper strips, secured with bolts, formed a direct connection between the upper and lower cavity plates, further enhancing thermalization.

The task of cooling the tuning rod posed a multifaceted challenge. Because the tuning rod must rotate smoothly and cannot be rigidly attached to other components, conventional cooling methods were rendered impractical. Furthermore, the substantial heat contribution of the tuning rod relative to its surface area potentially creates the so-called "hot-rod problem" [36]. To address this issue, we employed varnish and glue to create robust thermal interfaces between the upper cap of the tuning rod and the sapphire axle, resulting in improved thermal conductivity. To further enhance the thermal connection, copper braiding was employed to link the sapphire axle and the cavity's top plate. This braiding was secured with bolts and enveloped with varnish. To additionally stabilize the resonance frequency and diminish heat generated by vibrations, the sapphire axle connected to the bottom of the tuning rod directly touches the cavity floor with its end finished like a spinning top. Upon examination of the noise spectrum, we have determined that the hot-rod issue has been vastly improved. Although we observed a minor Lorentzian excess, it was attributable to the slight temperature variance between the MXC and the cavity, as per our analysis.

Notwithstanding the considerable size of our experimental cavity, we successfully crafted a ULC using OFHC copper. Our approach utilized various techniques, each designed to address specific thermal interfaces. This ULC allowed us to achieve a low cavity temperature of about 30 mK, marking a significant milestone in achieving one of the lowest-temperature and lowest-noise axion experiments to date.

B. Readout electronics

One critical element of CAPP-MAX's readout electronics is the low-noise amplifier, limited by quantum noise. The noise of these amplifiers is constrained by the uncertainty principle. Quantum squeezing technology [72] offers a way to overcome this limitation. However, this approach does not readily apply to measuring signals

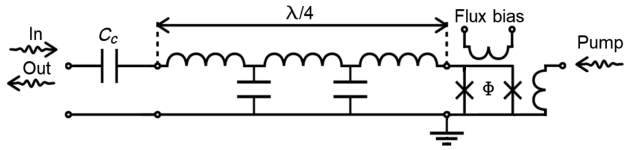

FIG. 6. Equivalent circuit diagram of a JPA. The magnetic flux bias defines the average inductance of the SQUID loop (the Josephson junctions are denoted as × in the loop), while the pump is modulating this flux at twice the frequency of the signal to be amplified. Since the signal in and out ports are the same, a circulator is needed to operate the amplifier [see Fig. 7(a)].

with a stochastic phase component, as it generally necessitates prior knowledge of the anticipated signal's phase [73]. Although the vacuum squeezing technique has been used in axion experiments to achieve a twofold gain in scanning rate [74] for frequencies exceeding 4 GHz, we have not yet implemented this technique in our work.

We utilize flux-driven Josephson parametric amplifiers [75] as quantum-noise-limited amplifiers for the faint signals from our haloscopes. The equivalent circuit of our JPAs includes a coplanar-waveguide $\lambda/4$ resonator that is grounded through a nonhysteretic superconducting quantum interference device (SQUID) (Fig. 6). This resonator is coupled to the external transmission line through a capacitor C_c. The signal input and output share the same port. The JPAs operate by modulating the SQUID inductance through an external pump signal. A SQUID acts as a nonlinear inductance whose value can be modulated by sending a pump signal through a line inductively coupled to it. The operating frequency can be tuned in a certain range by adjusting the average inductance of the SQUID by applying dc flux using a superconducting coil.

Our JPAs operate in the three-wave-mixing mode with the pump (f_p), signal (f_s), and idler (f_i) frequencies satisfying the relation [76]

$$f_p = f_s + f_i. \tag{5}$$

The JPA amplifies the signal injected from a source port and reflects it back. The source can be noise generated by either a wideband 50 Ω terminator or the cavity. The signal paths for both cases are shown in Fig. 7(a). A circulator is employed to separate the incoming and outgoing signals. The subsequent amplification is achieved by two HEMT amplifiers mounted at the 4 K stage of the fridge. Further signal processing is performed by a room-temperature amplifier and spectrum analyzer (SA) or a custom DAQ system.

In our experimental setup, we encounter the challenge of potential magnetic-field effects on various components, including circulators, isolators, HEMT amplifiers, and most importantly, the JPA. The magnet compensation region, which minimizes the impact of magnetic fields, is predetermined by the magnet manufacturer and may not

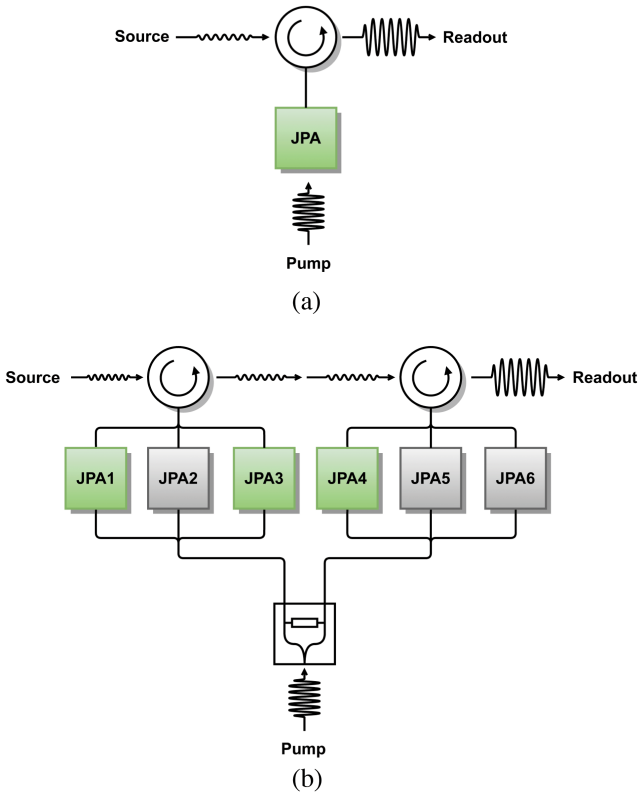

FIG. 7. Simplified diagrams of the JPA connection in the readout chain. (a) Single-JPA configuration used in runs 4 and 5. (b) JPA assembly used in run 6 with two holders connected in series. Each holder has the capacity to accommodate up to 3 JPAs. The green color indicates the current placement of JPAs, while the gray color represents blank positions reserved for three JPAs for future amplifier development. To minimize any potential interference between them, two of them were positioned in holder 1 and one in holder 2.

accommodate all the components in our setup due to space limitations.

To overcome this challenge, we employ shielded components, such as circulators and isolators, and have also developed custom shields (see Fig. 8) dedicated to safeguarding sensitive components.

To protect the JPAs from strong magnetic fields, we developed a multilayer nested shield [77]. The shield comprises three components, as shown in Fig. 9. The outermost layer is crafted from a superconducting NbTi alloy with a high critical magnetic field. The second layer is made of cryoperm alloy. Its purpose is to effectively redirect and absorb external magnetic fields, significantly diminishing the overall magnetic field intensity. Finally, the innermost layer is composed of a superconducting Al alloy, adding an extra layer of protection against magnetic field penetration.

In the initial conditions at noncryogenic temperatures, the superconducting shields exhibit behavior akin to nonmagnetic materials. The reduction of the initial

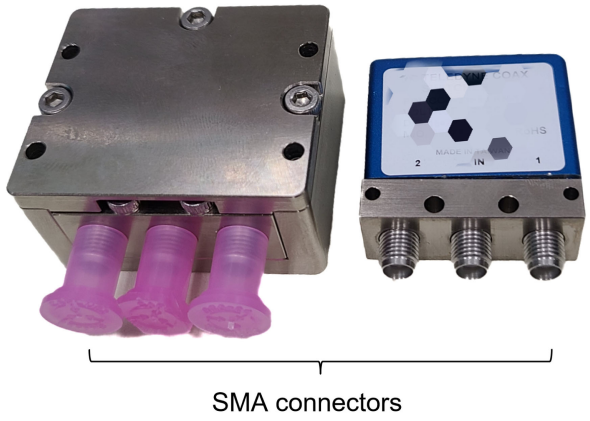

FIG. 8. rf switches with (left) and without (right) a magnetic shield.

magnetic field is accomplished by the second shield layer. During the cooling process, the first layer, constructed from a superconducting material with a high critical magnetic field, undergoes a transition from its normal state to the superconducting state. This transformation enables it to effectively trap the initial magnetic field within the shield. Meanwhile, the magnetic field within the second shield remains largely unaffected. As the temperature approaches the critical point for the innermost shield layer, it freezes the remaining magnetic field from the second shield.

In a detailed simulation using the ANSYS electronics desktop [78], it was found that the magnetic field within the shield dropped to below 100 nT when exposed to an external field ranging from 0 to 0.1 T, as shown in Fig. 9. The simulation is confirmed by a measurement at 4 K [77].

The magnet's residual field at the JPA position, without the shield, measures approximately 0.01 T. With the implementation of this shield, the field strength at the JPA is effectively reduced, giving a small shift of the JPA dc bias as shown in Fig. 10 for 10 times as much (0.1 T) external magnetic field. The corresponding shielding factor is estimated between 10^5 and 10^6.

While the flux-driven JPA offers extremely low noise close to the quantum noise limit, its original design had a limited tuning range of 45–60 MHz [77]. In runs 4 and 5 we successfully used one amplifier to scan 20 and 58 MHz, respectively [32]. This presented a challenge for CAPP-MAX as it required frequent warm-up and replacement, resulting in significant time loss and the consumption of large amounts of LHe. Our cavity possesses a tunable range of 200–300 MHz, and the scanning range of each run was determined by the tuning capabilities of the JPA. Therefore, our primary goal was to extend the amplifier's range without compromising the exceptional noise properties of our JPAs. To achieve this, we employed two methods, which we recently reported: serial and parallel connections of the JPAs [79].

During run 6, we used a combination of parallel and serial connections, using holder 1 with two JPAs and holder 2 with one JPA; see Fig. 7(b). Holder 1 encompasses JPAs designed for frequency ranges of approximately 1.080–1.122 and 1.135–1.183 GHz, while holder 2 houses a JPA with a tunable range spanning 1.045–1.070 GHz. To accommodate three JPAs within a single holder, we designed a specialized printed circuit board (PCB), as illustrated in Fig. 11. During operation, only a dedicated JPA is activated, with the other two being disabled by adjusting the resonance frequency. Experimental results demonstrate that all three JPAs operate effectively without

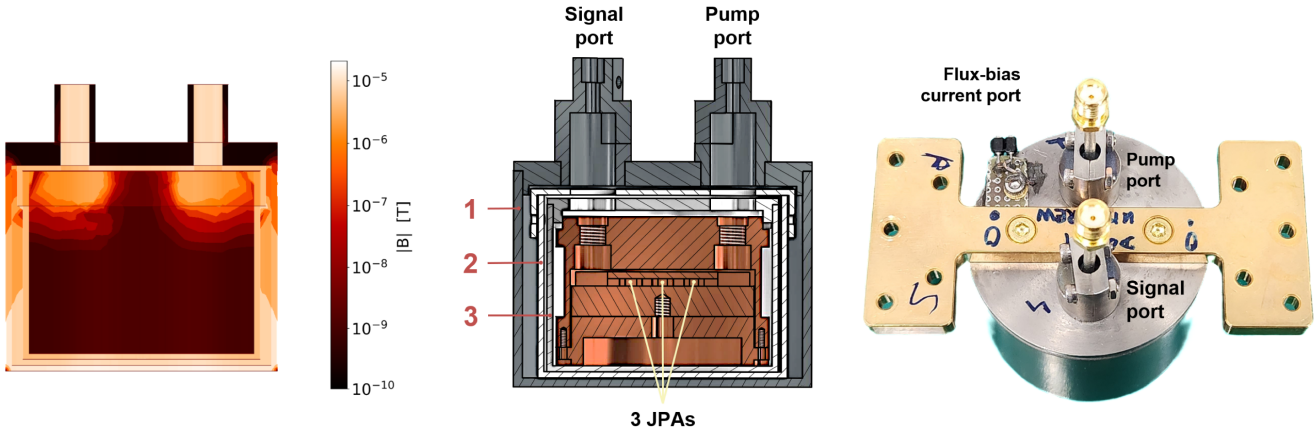

FIG. 9. Three-layer magnetic shield for a JPA. (a) Simulated magnetic field map inside the shield under an external background of 0.1 T. (b) Drawing of the cross-sectional view of the shield: Each layer, from the outside to the inside, is made of NbTi (1), cryoperm (2), and Al (3), respectively. (c) Photograph of the assembly with the SMA connectors shown.

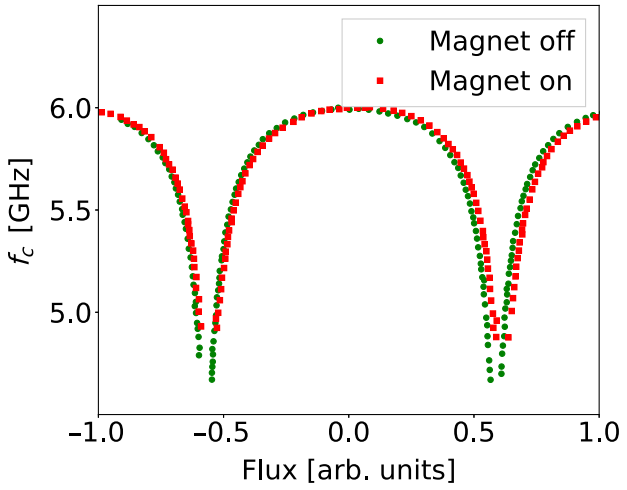

FIG. 10. Dependence of resonance frequency (f_c) in a passive mode of the JPA on applied dc flux bias, as measured with a separate device with the resonance frequency at 6 GHz. The two colors correspond to the data taken in the presence and absence of the residual magnetic field of 0.1 T, which is 10 times higher than expected during axion search experiment.

compromising their noise characteristics. There was an overlap in frequencies between runs 5 and 6. To enhance sensitivity, we combined the shared data from these runs.

Our setup has the capacity to incorporate up to 6 JPAs through a combination of both parallel and serial connections [80]. For our upcoming run 7, we are using 6 JPAs

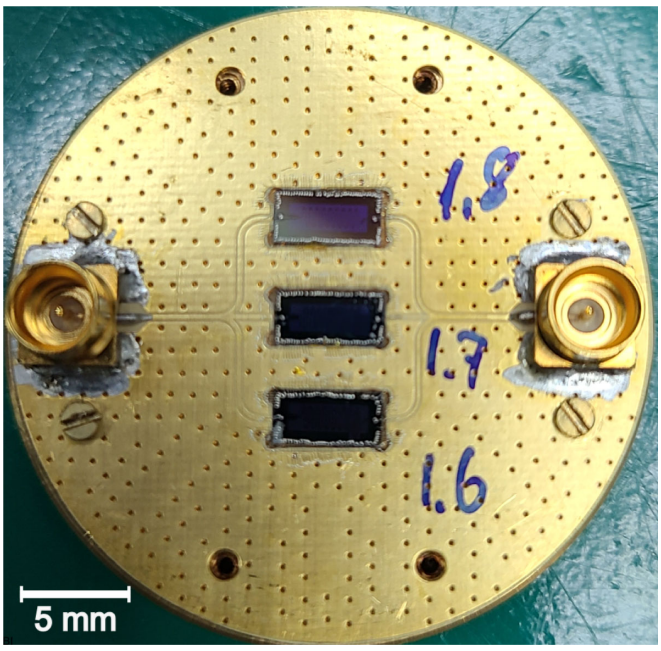

FIG. 11. Top view of the gold-plated PCB with three JPA chips bonded. The pump and signal lines are connected through Sub Miniature version P (SMP) connectors. The diameter of the PCB is 30 mm, and the area of the chip is 2.5×5 mm^2.

covering a total range of approximately 300 MHz from 1.2 to 1.5 GHz [79].

The readout electronics diagram is depicted in Fig. 12, providing an overview of the experimental setup used for all characterization measurements and the running of the experiment. The diagram displays various temperature stages, beginning from room temperature (300 K), 4 K, 1 K, cold plate, and mixing chamber plate. Each temperature stage includes an attenuator for each rf line to prevent Johnson noise due to higher temperature stages from affecting the colder stages.

The setup is not only designed to conduct experiments but is also suitable for characterizing our JPA. In terms of noise characterization, our setup incorporates a noise source (NS) that enables the measurement of noise temperature for both the JPA and the HEMT.

Facilitating noise checks, cavity tests, and experiments, a cold rf switch is integrated within the setup. This rf switch enables seamless switching between the noise source and the cavity. Additionally, the rf switch features an intermediate state that allows for the measurement of line losses between the cavity and the switch, as detailed in Ref. [32].

The JPA signal is amplified using low-noise cold HEMT amplifiers. Two HEMT amplifiers LNF-LNC0.6_2A [81] are connected in series and thermally stabilized at the 4 K stage of the refrigerator. To mitigate the adverse effects of signal reflections from the amplifier, an isolator is placed between the JPA assembly and the HEMT. This isolator is thermally anchored to the fridge cold plate. Temperature sensors attached to the amplifiers are used to monitor the enclosure temperature, which typically reads 5 and 6 K during operation at optimal voltage and current biases while the fridge is operational.

To measure the noise temperature of the HEMT amplifiers, we employed a methodology similar to the widely used Y-factor method [82]. We use a single-channel noise source. The NS consists of a wideband matched 50 Ω terminator, a heater, a thermometer, and 9-pin Micro-D connectors for the thermometer and heater. These components are assembled on a gold-plated copper holder (see Fig. 13) and are specifically designed to be installed on the mixing chamber rf assembly. In our test fridge, we utilize a four-channel version of the NS described in Ref. [83].

The NS is connected to the measurement chain using a 0.047-in.-diameter NbTi microwave coaxial cable, which is superconducting below 11 K and provides excellent thermal isolation between the NS and other circuits. The NS and the NbTi cable are placed in a space where the field is reduced to below 0.05 T by a compensation coil provided by the superconducting magnet manufacturer (see Fig. 1). This setup ensures that the magnetic field will not affect the properties of the NS and the cable. The system noise temperature was measured with the magnet on and off, and

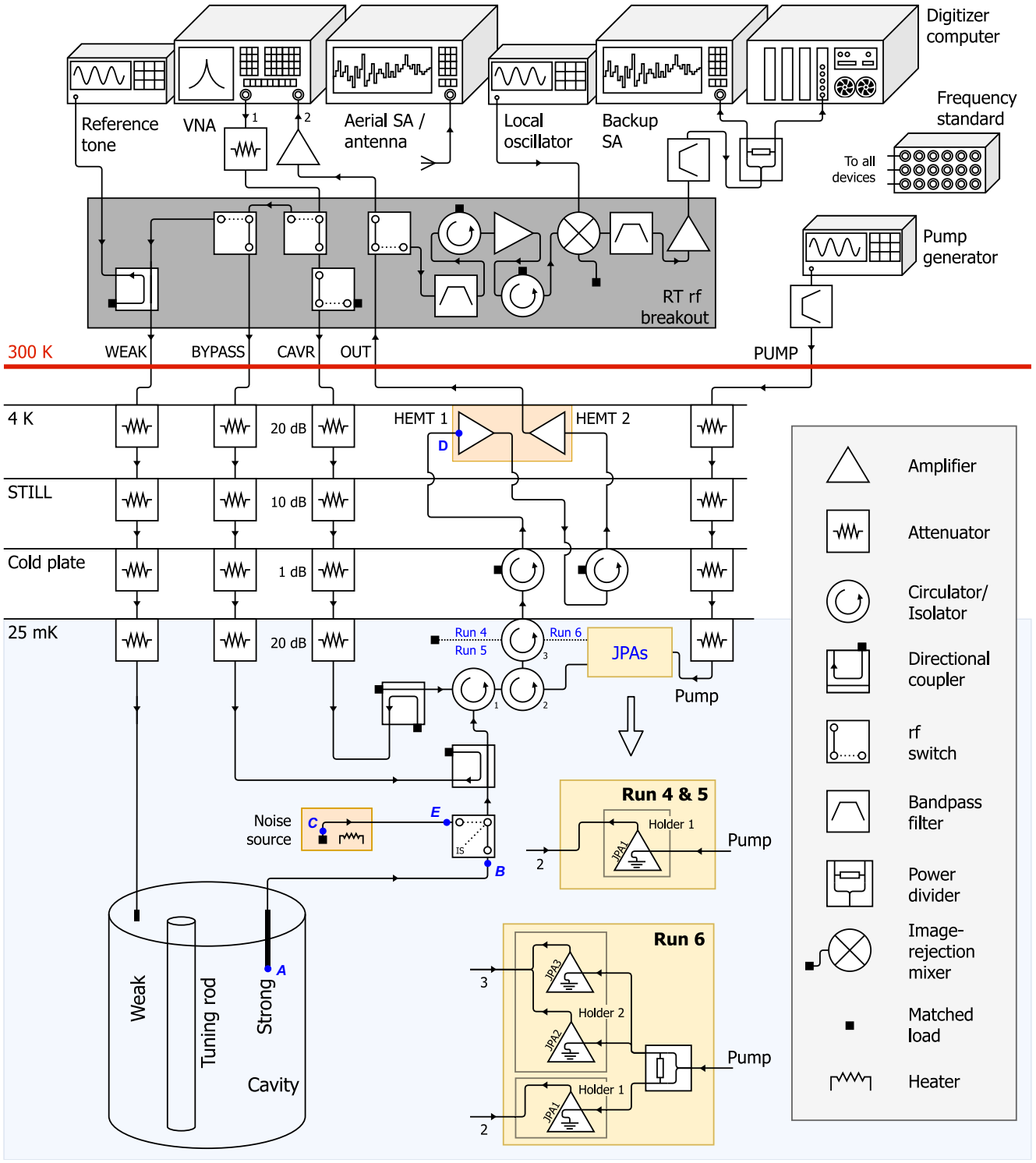

FIG. 12. Experimental setup including the cavity, a cryogenic receiver, measurement chains, and the room temperature DAQ system. The major components of the receiver chain are JPAs, a three-junction circulator or isolator, and a series of HEMT amplifiers (HEMT1 and HEMT2). The chain has two JPA configurations for two data taking runs, runs 4 and 5, and run 6. The cavity properties are measured through several lines: weak cavity coupler (WEAK), bypass cavity test (BYPASS), and cavity reflection (CAVR). The DAQ system consists of a radio-frequency signal generator (rf generator), a VNA, an SA, a radio-frequency local oscillator (LO), an image-rejection mixer (IRM), and a digitizer. The noise source is used in the noise-temperature calibration of elements in the rf-measurement chain. Typical values of attenuators are shown on the CAVR line, and are similar for those on the same temperature plate. Transmission coefficients between reference point A–B and C–D are defined as η_c, η_u, respectively; see text.

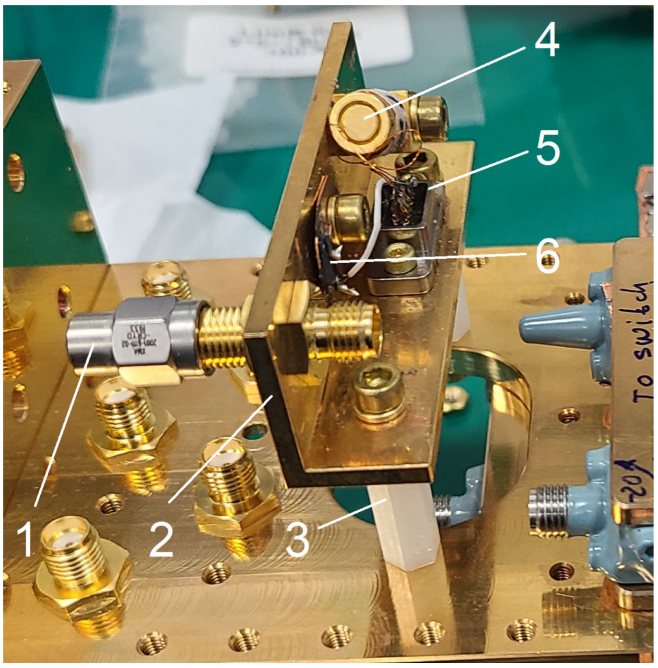

FIG. 13. rf-noise-source assembly. (1) 50 Ω terminator connected to SMA bulkhead, (2) enclosure, (3) thermally isolating plastic stand, (4) thermometer, (5) dc connector, and (6) heater. The assembly is weakly thermally anchored to the MXC by a thin copper wire (not shown).

observed to remain the same as long as the JPA assembly and the cavity were maintained at the same operating temperatures.

Superconducting NbTi twisted pair cables with negligible thermal conductivity are used to connect the temperature sensor and heater. The temperature sensor is a calibrated RuO_2 sensor produced by Lake Shore Cryotronics, and the heater is a metal-film 100 Ω resistance that maintains stability within 1% over a wide temperature range, from room temperature to the base temperature of the MXC.

For precise temperature measurement and control, we utilize the 372 ac resistance bridge and temperature controller provided by Lake Shore Cryotronics. The NS is securely fixed to the MXC assembly using two 20-mm-long plastic spacers, and thermal anchoring to the MXC plate is achieved through a 15-cm-long copper wire (see Fig. 13).

The ports Bypass and Output (see Fig. 12) were used for direct measurements of the JPA characteristics that effectively bypass the cavity. To assess the noise level of the HEMT amplifier, we deactivated the JPA pump signal and adjusted the dc flux bias current to shift the passive resonance of the JPA away from the measurement frequency. In doing so, the JPA behaves as an almost ideal reflector, causing estimated losses of less than 0.2 dB around 1 GHz [57], thereby minimizing its influence on other circuits within the setup.

Subsequently, we proceed to establish and stabilize the temperature of the noise source at a specific value. We then measured the power spectral density (PSD) within the desired frequency range. This process is repeated for 3–4 different temperature settings, allowing us to acquire a range of PSD values corresponding to various noise temperatures.

The measurement of JPA noise can be accomplished using the modified Y method, as described earlier in this paragraph and in Refs. [31,57]. However, this method has some drawbacks, including the lengthy setup and cooling time required for the noise source and the potential for saturation due to the limited dynamic range of the JPA. To address these challenges, we employ a spectrum comparison method. In this approach, we compare the SNR with the JPA turned off to the SNR with the JPA turned on. This method provides a more time-efficient measurement technique to assess the noise characteristics of the JPA [34]. The result of the direct Y-factor method on the JPA for a limited temperature range is consistent with that of the SNR-comparison method. Our flux-driven JPAs demonstrate noise levels 1.9–3.6 times the quantum noise limit for amplifier added noise for the frequency range of 1–2 GHz, as reported in Refs. [77,79,80,84].

For the frequency range of 1–2 GHz, the quantum noise limit ranges from 48 to 96 mK, while the minimum added noise due to the amplifier increases from 24 to 48 mK. This highlights the significance of cooling all the readout components of the initial stages to temperatures below these limits in order to achieve the lowest possible system noise temperature.

At temperatures below 100 mK, certain effects and phenomena become more pronounced, which are usually hidden by the thermal motion of the particles at higher temperatures. Among these effects, acoustic mismatch [85,86] and electron-phonon decoupling play a significant role. Also, phonon thermal conductivity decreases as a result of the reduction in the number and energy of phonons. Thus, it is advisable to avoid dielectrics during thermalization, even layers of oxides that form on metals.

By employing metal interfaces and applying a gold coating between the mixing chamber and the various parts and components installed on it, we successfully achieved notably low temperatures for the cavity, JPA, and cold rf components in our axion experiment, reaching 22–25 mK. This approach led to a reduction in the total system noise, bringing it as low as 200 mK, or about 4 SQL, in the CAPP-MAX experiment.

IV. DATA ACQUISITION AND MONITORING

As shown in Fig. 14, most of the instruments are connected to the main DAQ computer over Ethernet within a local network. Others are directly connected to the main DAQ computer via the universal serial bus (USB) and the recommended standard 232 (RS-232). An additional

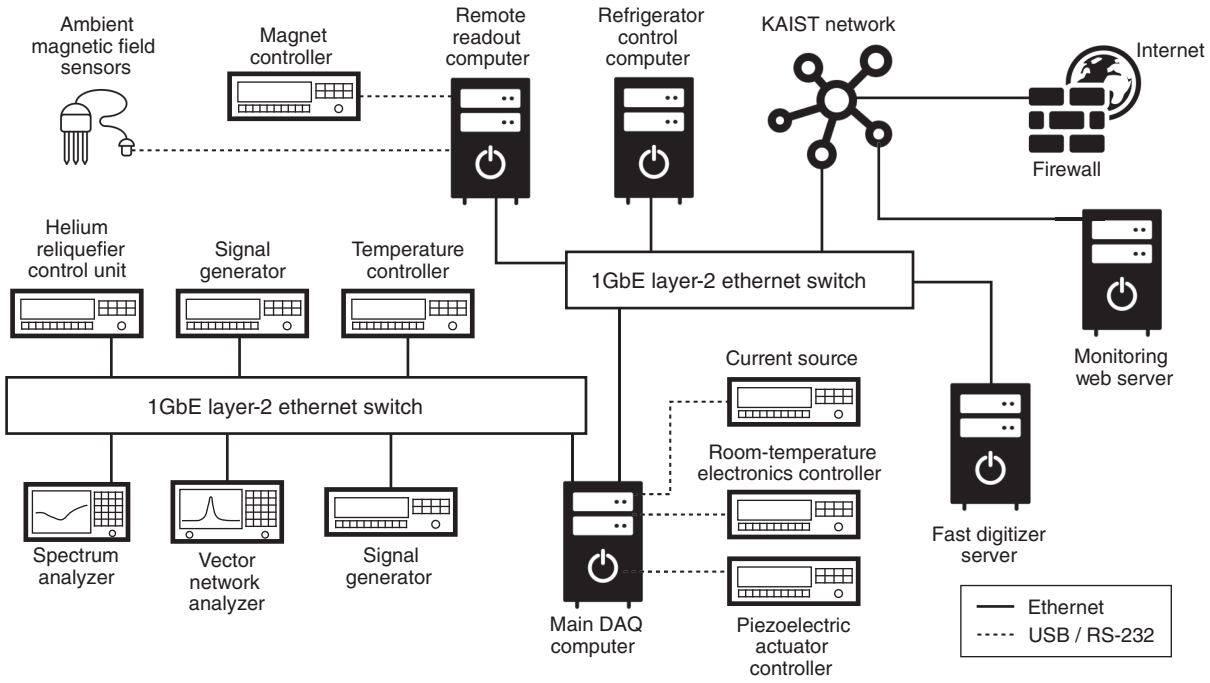

FIG. 14. Instrument connections for data acquisition. Most instruments are connected to the main DAQ computer via either Ethernet (solid line) distributed by Ethernet switches or USB/RS-232 (dashed line) directly.

readout for the magnet information and measurements of the ambient magnetic field around the system is also connected over Ethernet. Finally, a dedicated computer for controlling a fast digitizer is connected over Ethernet as well.

The DAQ is governed by a home-developed data acquisition software, CULDAQ [87]. The software provides features of controls over devices in the experiment via various communication protocols, data readout and packaging, storing monitoring data, and experiment run sequence. In the DAQ software, there are three layers of classes for the device controls: abstract classes to support communication protocols such as Ethernet, USB, RS-232, and so on; wrapper classes that translate the standard commands for programmable instruments or instructions provided by the manufacturers into user-friendly functions; classes providing higher level functions that utilize and combine a set of functions implemented in the wrapper classes to perform practical tasks conveniently. This hierarchy of classes keeps the software in a modular structure and provides a good reusability and readability of the code. The software also provides utility classes for the convenience that support database access, logging, and data packaging. The data acquired in the experiment are packaged in a ROOT format [88]. The data read by a fast digitizer are also packaged as separate ROOT files, and the former ROOT file contains a map to match the experiment runs to the fast digitizer data. In addition, critical information for the experiment operation such as the total system physical temperatures, pressures, and magnetic fields are recorded in a database so that an online monitoring is available during the experiment.

When the components implemented in the software are combined, a logical sequence of the experiment can be formed. An experiment sequence requires a set of configuration parameters such as a frequency tuning range and step, a number of spectra to be averaged, parameters of instruments (center and span frequencies, resolution bandwidth, and so on), and they are given in the beginning of a measurement. A typical experiment sequence is as follows.

(1) Initializing the instruments by the given parameters.
(2) Tuning of the cavity resonant frequency to the initial target frequency.
(3) Measuring the auxiliary data such as the system physical temperatures, pressures, magnetic field, and so on.
(4) Tuning of the JPA at the current resonant frequency and a target gain.
(5) Characterizing the cavity by measuring the cavity reflection and transmission.
(6) Characterizing the receiver chain with turning on and off the JPA.
(7) Taking power spectrum data for about 192 s with a fast digitizer (high efficiency) and a spectrum analyzer (for consistency checks).
(8) Characterizing the cavity again.
(9) Measuring the auxiliary data again.
(10) Tuning the cavity resonant frequency to the next target frequency, with a step of about 10 kHz, and repeating the sequence from 3.

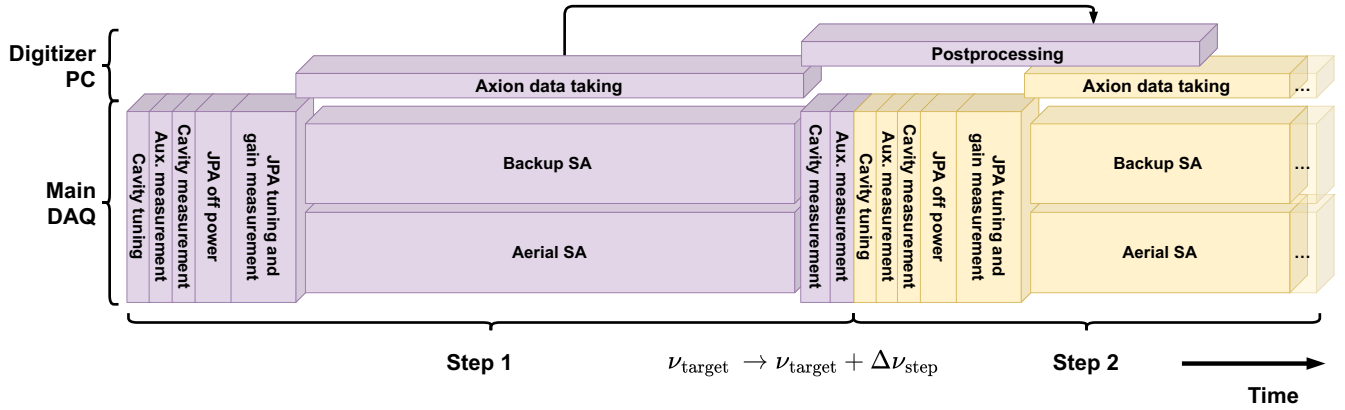

FIG. 15. Measurement sequence during data taking. It includes physics data taking, cavity measurement, and system noise calibration. ν_{target} is the target frequency that the resonance frequency of the cavity and the JPA (with −100 kHz offset) is tuned. $\Delta\nu_{\mathrm{target}}$ is the frequency tuning step, which is kept 10 kHz throughout the data collection. The acquisition time with the digitizer (Axion data taking period) is 192 s.

The sequence diagram is depicted in Fig. 15. Power spectrum data are taken using a fast digitizer. In addition, we acquire a small data sample simultaneously with a spectrum analyzer for consistency checking. We employ an M4i.4480-x8 manufactured by Spectrum Instrumentation GmbH [89] as the fast digitizer. For the experiment, we implemented the fast digitizer with a sampling rate of 45 MSamples/s and a resolution bandwidth of 10 Hz; therefore, the acquired data are capable of searching not only for virialized axions, but also for nonvirialized axions [58]. The practical DAQ efficiency of the fast digitizer approaches 100% [90].

The total scanned frequency range within runs 4–6 with different rf configurations in Fig. 12 is shown in Fig. 16. Runs 4 and 5 were taken with a single JPA while run 6 utilizes 2 JPA holders with a total of 3 JPA chips.

V. ANALYSIS AND RESULTS

To confirm the integrity of these data, a parallel system using a commercial spectrum analyzer is also used in the data stream. In addition, a second spectrum analyzer is used to collect data using an aerial antenna tuned to the frequency of interest in order to detect unwanted interference from outside [91]. Those interference signals are usually narrower than those expected from standard halo axion dynamics, but perhaps compatible with narrow axion lines that appear as transients due to the focusing effects of the Sun, moon, planets, and Earth itself [48,92–96]. One such signal is shown in Fig. 17. The signal was intermittent and appeared simultaneously at the SA connected to the aerial antenna, indicating external interference. It was most likely due to a radio communication with approaching aircraft into a nearby airport using the same frequency [97].

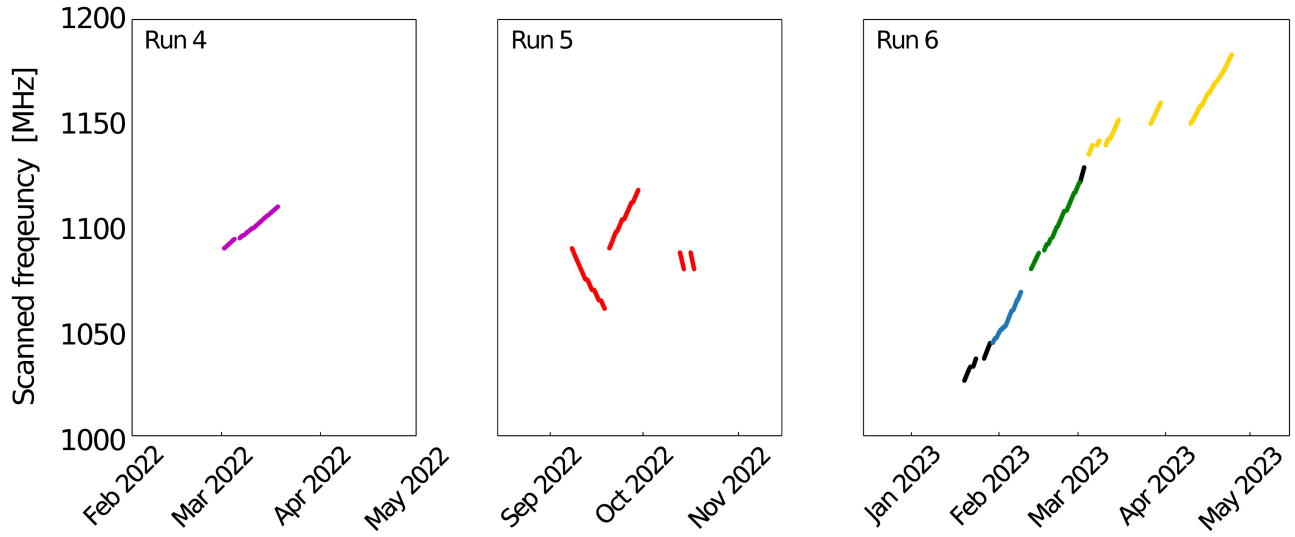

FIG. 16. Scanned frequency as a function of calendar time for runs 4–6. Different colors represent different JPAs, except black, which corresponds to the scan with no JPA operating in the rf chain.

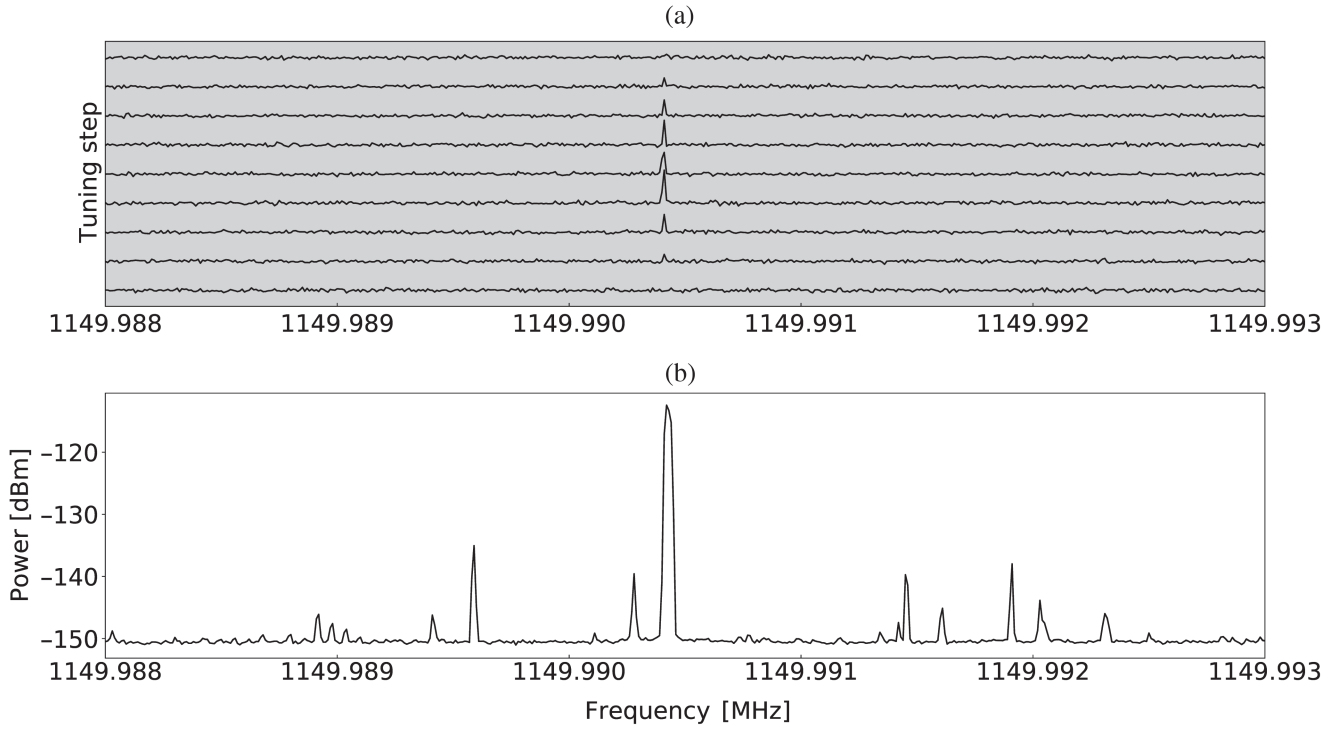

FIG. 17. (a) Candidate signal with a large SNR. It shows the noise power data after the normalization procedure given by Eq. (10). Each spectrum represents the data taken at each DAQ step. From the bottom to the top spectra, the cavity resonance frequency is tuned from left to right with roughly 10 kHz step. The fourth spectrum from the bottom is taken when the cavity is tuned to nearly 1149.99 MHz, which is closest to the signal among the steps. Since the normalized power excess of the signal gets higher as it gets closer to the resonance frequency of the cavity, the signal is thought to appear in the cavity. (b) The power spectrum taken with the aerial antenna connected to a spectrum analyzer. The signal is finally rejected based on the aerial frequency and time spectra. The frequency and width of the signal are approximately 1149.9905 MHz and 20 Hz, respectively.

Figure 17 shows the main analysis strategy for signals with a large SNR ratio. The criteria for considering those signals as candidates are as follows.

(1) The signal amplitude needs to follow the cavity response, and
(2) the signal needs to be absent from the spectrum analyzer connected to the aerial antenna.

If those conditions are met, we acquire more data for a long time, enough to establish the stability of the signal as a function of time. If other modes than the TM_{010} are close to the candidate frequency, the cavity is tuned to that mode as well [35]. If all is consistent with the signal being an axion, the final check is testing its magnetic field dependence. The rest of the signals with small SNR require more steps to optimize signal detection. The overall data-analysis steps are shown in Fig. 18 and are described in detail below. The flow of the analysis is similar to the procedures described in Refs. [32,98–101]. The goal is to construct grand spectra where the candidates for rescan can be classified or the exclusion limit can be set. The underlying probability distribution of the noise fluctuation is Gaussian, as a large number of spectra are averaged together. Unbiased combination procedures throughout the analysis guarantee that the final product of the analysis also yields a standard normal distribution, by properly normalizing the uncertainty and compensating for the mean offset. The grand spectra from predefined subsets and their rescan datasets are aligned and combined using the Bayesian power measured (BPM) analysis framework [102].

The first step of the analysis involves the estimation of the SNR of the axions with an arbitrary coupling strength g_γ at each data point. This step plays two important roles. First, the SNR is used for estimating the experimental sensitivity on the axion–photon coupling g_γ. Next, it is used as a weighting factor for optimal combination of the data where axions possibly exist. As defined in Eq. (3), it requires the axion-to-photon conversion power and the system noise temperature at each frequency.

The conversion power depends on experimental parameters such as the cavity bandwidth $\Delta\omega_c$, resonance (angular) frequency ω_c, loaded quality factor $Q_l = \omega_c/\Delta\omega_c$ of the cavity, coupling coefficient of the strong antenna β, as well as the external magnetic field $\mathbf{B}_e$ inside the cavity volume V and the form factor of the TM_{010} mode. The loaded quality factor, the resonance frequency of the cavity, and the antenna coupling are obtained using the real and

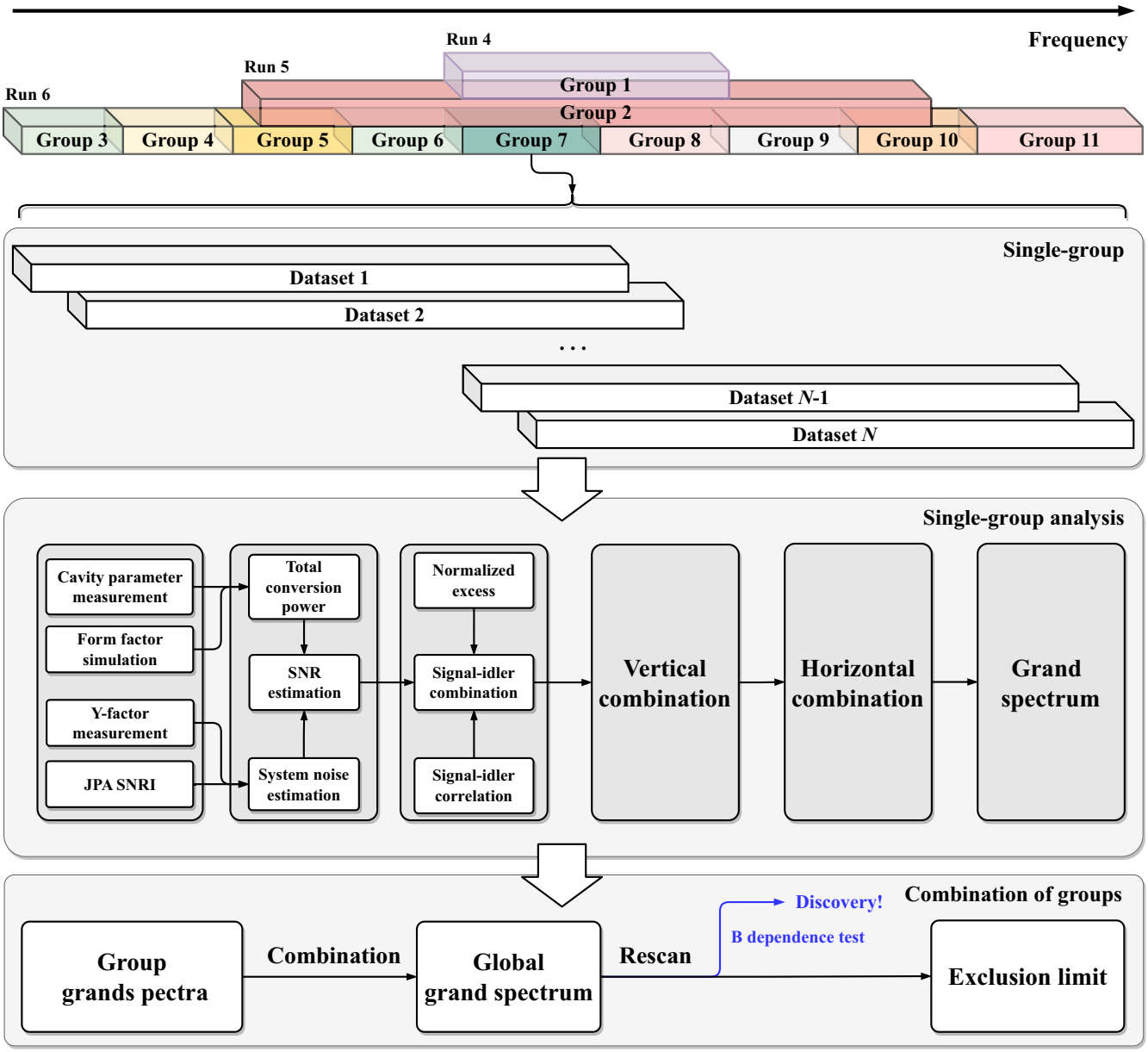

FIG. 18. Overview of the analysis procedures in three different runs (runs 4–6). The group refers to a bundle of the dataset within approximately the same statistical characteristics. Each group of data is processed according to the steps outlined in the single-group analysis part. Subsequently, the resulting grand spectra are optimally combined in order to construct the global grand spectrum. Rescan candidates are identified based on this grand spectrum for additional statistical testing.

imaginary part of the complex S parameter through the reflection line. $\mathbf{B}_e$, V, and the form factor are obtained from simulation using COMSOL MULTIPHYSICS [67], together with the magnetic field profile, which is a simulation result provided by the manufacturer [56]. Q_l and β are found to vary between 35000 and 55000 and 1–2, respectively. The coupling β is adjusted only a few times during data collection to keep it within that range. The scanning speed is optimal for $\beta = 2$, and it remains quite flat around that value. However, operating the coupling adjustment system caused a temperature increase, so we avoided doing it frequently.

The system noise temperature calibration is started with the noise temperature measurement when the JPA pump is off and far detuned from the measurement range. The cryogenic switch is toward the noise source in order to measure the noise power depending on the NS temperatures, and therefore it refers to point C in Fig. 12. The noise power $P_{\mathrm{off}}^{\mathrm{NS}}$ measured with the digitizer in this configuration is modeled as

$$P_{\mathrm{off}}^{\mathrm{NS}} = k_B \Delta\nu_b G_{\mathrm{off}}(T_{\mathrm{NS}} + T_{\mathrm{off}}), \tag{6}$$

where $\Delta\nu_b$ is the resolution bandwidth of the measurement and T_{NS} is the effective noise temperature given by the matched load of the NS, including the vacuum contribution. T_{off} is the noise temperature referenced to the NS, which includes the loss factor η_u between points C and D in Fig. 12. $P_{\mathrm{off}}^{\mathrm{NS}}$ is measured at more than three different temperatures of the noise source, and then the P_{off} versus $T_{\mathrm{NS}}^{\mathrm{eff}}$ graph is fitted using Eq. (6) to estimate T_{off} and G_{off}. η_u is not measured directly since its effect is included in T_{off}. From the gain and noise specifications of HEMT 1 and HEMT 2, it can be roughly calculated to be between 0.5 and 5 dB depending on the frequency. For a given NS temperature, P_{off} spectra are measured with sweeping LO frequencies in order to keep an intermediate frequency of 10.7 MHz for the digitizer. In practice, it is done with 1-MHz frequency step for a given fraction of the scan range. After the data acquisition is finished and a scanning of ~10 MHz is accomplished, the whole process is repeated in order to update the T_{off}, which is slowly drifting due to HEMT amplifiers' gain stability limitations. Overall, T_{off} varies between 1.5 and 4 K range, with the maximum around 1130 MHz.

For the next step of the calibration, we measure *in situ* the SNR improvement (SNRI) [34] during the data taking, when the cryogenic switch is toward the cavity. We compare two states: (1) the JPA and the cavity are tuned at the target frequencies and the JPA pump is on (JPA on), and (2) the JPA passive resonance and the cavity are detuned far away from the target frequencies and the JPA pump is off (JPA off). The SNRI is defined as

$$\mathrm{SNRI} = \left(\frac{G_{\mathrm{on}}}{P_{\mathrm{on}}}\right)\left(\frac{G_{\mathrm{off}}}{P_{\mathrm{off}}}\right)^{-1} = G_J/r. \tag{7}$$

P_{on} (P_{off}) and G_{on} (G_{off}) are noise power and gain when the JPA is on (off). Those spectra are taken in every step of the data acquisition as described in Fig. 14. After reorganizing the equation, $r = P_{\mathrm{on}}/P_{\mathrm{off}}$ is defined as the ratio spectrum, and $G_J = G_{\mathrm{on}}/G_{\mathrm{off}}$ as improvement of signal power when the JPA is on, which is typically around 50 at the resonance frequency of the cavity. G_J can be further expressed as $|S_{21,\mathrm{on}}|^2/|S_{21,\mathrm{off}}|^2$, where S_{21} is the S parameter measured through the bypass line. In practice, instead of tuning the cavity outside the measurement range, we fit P_{off} and $|S_{21,\mathrm{off}}|^2$ spectra by excluding the data around the resonance frequency of the cavity. By setting the JPA off state in this particular way, it does not involve the thermal noise from the cavity, whereas it is included in the JPA on state. Including the cavity in both states could also lead to correct results, once the cavity temperature and the coupling effects are taken into account correctly [103]. In our case, a naive approach would lead to a slightly lower system noise temperature by a few percent.

The system noise temperature can be calibrated using the SNRI and a reference JPA off noise temperature. The reference noise temperature can be obtained using T_{off}. As the switch is toggled from the noise source to the cavity, an additional loss factor η_c between the reference point A and B must be considered. The loss between the reference point B and D is approximately equal to η_u, by considering the fact that the line between point C and E is a superconducting rf cable. η_c is estimated using the intermediate state as discussed in Ref. [32]. It is found to be 0.932 ± 0.003 under the assumption that it is frequency independent within the frequency range of the data taking.

The reference noise temperature when JPA is off therefore can be expressed as

$$T_{\mathrm{ref}} = \frac{T_{\mathrm{off}} + T_{\mathrm{MXC}}^{\mathrm{eff}}}{\eta_c}. \tag{8}$$

T_{ref} is the reference noise temperature, $T_{\mathrm{MXC}}^{\mathrm{eff}}$ is the effective noise temperature from components thermally anchored to the mixing chamber. $T_{\mathrm{MXC}}^{\mathrm{eff}}$ is dominated by the matched load on the directional coupler installed on the reflection line, followed by the loss of the three junction circulators [104]. Therefore, we use the temperature read from a sensor installed on the mixing chamber extension plate for $T_{\mathrm{MXC}}^{\mathrm{eff}}$. The uncertainty of $T_{\mathrm{MXC}}^{\mathrm{eff}}$ is taken into account in the total systematic-error estimation.

Using the SNRI and the reference noise temperatures, the total system noise temperature can be expressed as

$$T_{\mathrm{syst}} = T_{\mathrm{ref}}\frac{r}{G_J}. \tag{9}$$

T_{syst} around the resonance frequency of the cavity is found to be 200 and 250 mK on average in runs 4 and 5, respectively, as shown in Fig. 24. In run 6, it varies from 200 to 600 mK with JPA, and from 2 to 4 K without the JPA. The system noise temperature in run 6, especially in the region where the JPA is more sensitive to the external magnetic flux, is found to be higher than others, due to instability of the JPA gain in the specific frequency range.

For the case when the JPAs are not involved, Eq. (8) is used for the estimation of T_{syst}. To incorporate the effect of the thermal excess around the resonance of the cavity, P_{off} is first divided by the baseline obtained without the cavity region as discussed above. Then the divided spectrum is fitted again with a circuit model including the cavity [105]. The fitted model is multiplied by T_{ref} to define T_{syst}.

The baselines of the ratio spectra r and the JPA gain G_J are estimated in order to reduce the statistical uncertainty and also to define the normalized excess. To obtain r and G_J, the baselines of P_{off} and $|S_{21,\mathrm{off}}|$ are used in order to reduce the statistical uncertainty, and also to preserve the Gaussian distribution of the spectral fluctuation in r. Then for the ratio spectra, five neighboring frequency bins are

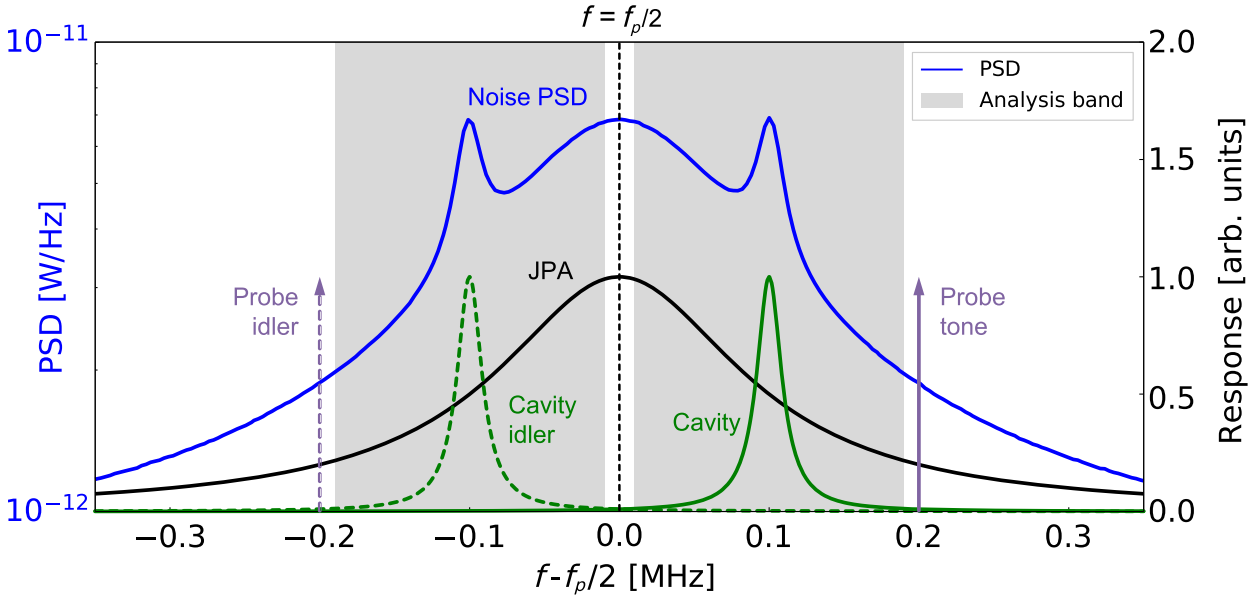

FIG. 19. Example of the noise PSD (blue, real data) and frequency responses of the JPA (black, simulated data) and the cavity (green, simulated data) as a function of the offset from the half pump frequency ($f_p/2$). The total gain is ~110 dB and the frequency responses are normalized to their maximum value. The spectrum shown on the left is mostly the image of the right-hand side spectrum due to the idler effect. We use this difference to further reduce the total system noise (see Appendix C). The probe tone (purple) injected through the weak port of the cavity is used for cross-checking and systematic-error estimation. The dashed lines represent the idler modes. Since the axion signal also appears on the idler side, the frequency bands (gray) on both sides are included in the analysis. The vertical scale of green, purple, and black lines is corresponding to the right-hand y axis with each normalized to itself independent of each other.

merged. Of the 1-MHz range, we utilize 360 kHz of the data; 180-kHz range of the data around the resonance frequency of the cavity and the same for the range around its idler frequency. The JPA essentially yields a highly symmetric output around the half pump frequency, owing to its three-wave-mixing property as described in Eq. (5) [57]. Using this fact, both spectra are decomposed into their symmetrical and asymmetrical parts. Each part in each spectrum is fitted individually, then combined as the final baseline.

The normalized power excess δ is defined using the ratio spectrum and its baseline:

$$\delta = \frac{r - b_r}{\delta r} = \left(\frac{r}{b_r} - 1\right)\sqrt{N_{\rm av}}. \tag{10}$$

$\delta r = b_r/\sqrt{N_{\rm av}}$ is the expected standard deviation of r by the central limit theorem, where $N_{\rm av}$ is the number of averages and b_r is the baseline of the ratio spectrum. Thus δ is expected to follow the standard normal distribution, which leads the reduced χ^2 goodness of the fit to have a mean of 1. Throughout the data, normalized excesses satisfy these expectations within the margins of error.

The combination process starts with the signal and idler sides of the data, shown as the gray area in Fig. 19. The SNR in the signal (R_S) and the idler (R_I) sides can be defined using the system noise temperature on each side of the data. Equation (9) is also used for the idler side, but with the JPA gain for the idler mode $G_I = G_J - 1$. The JPA-induced correlation between the two analysis bands is considered in optimizing the weights and the error combination. Then, the spectra are optimally weighted by their expected SNR to be summed vertically.

After vertical combination, the SNR of the virialized axion, dispersed in a bandwidth of around 5 kHz, is combined horizontally according to Refs. [22,100]. Since the axion mass is unknown, the combination is repeated for each axion rest-mass frequency. The effect of a mismatch between the axion frequency and the closest frequency point is found to be negligible because the resolution bandwidth used is much smaller than the axion line shape. To account for the variation at different axion masses, the line shape is evaluated at every 1 MHz.

The combined spectrum is normalized once more by dividing its standard deviation and subtracting its mean for the purpose of constructing a grand spectrum. In run 6 the standard deviation is found to be frequency dependent and is mostly larger than expected from simulation. For this reason, the data taken in run 6 are divided into 9 different groups, where the standard deviation is approximately uniform within each group. The group grand spectra are obtained from their own means and standard deviations, then they are vertically combined once more to construct a single grand spectrum. Rescan candidates are defined based on the 3.718σ threshold given by 90% confidence level for a target SNR of 5σ. For large narrow peaks, we follow the

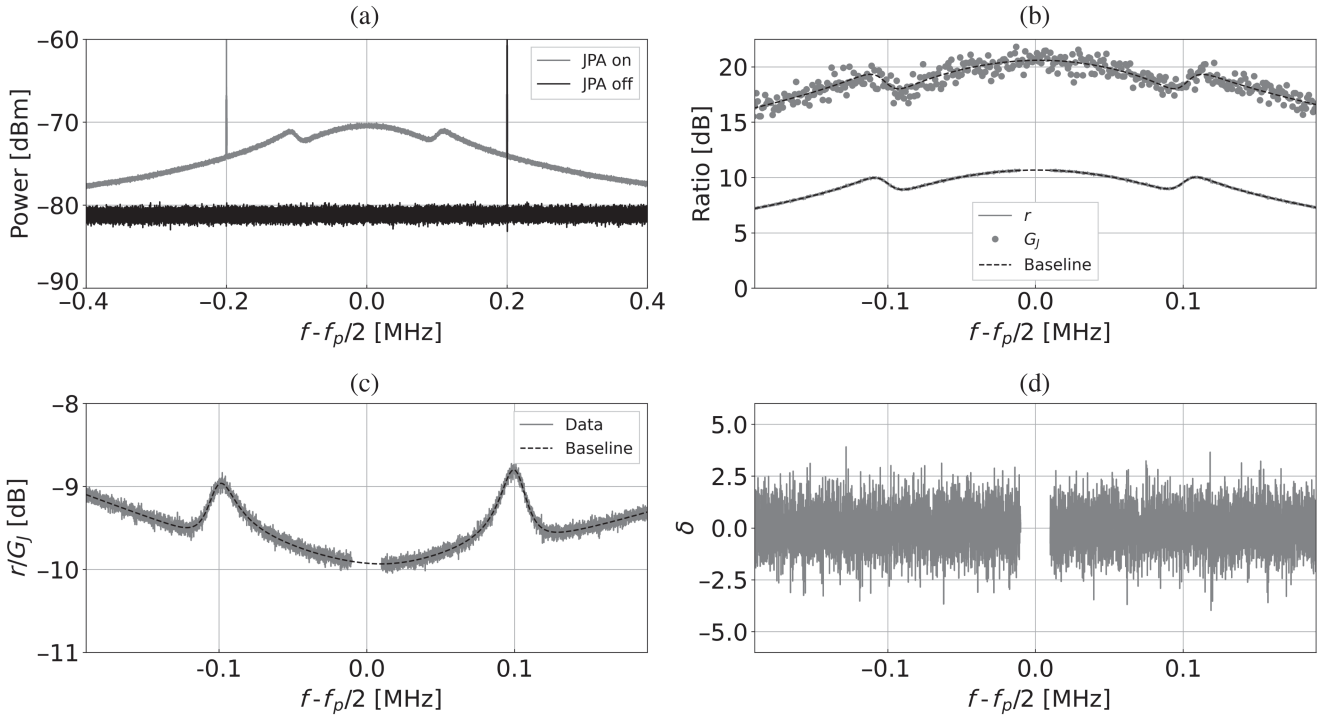

FIG. 20. Example of SNRI calibration and spectrum normalization. The spectra center ($f_p/2$) is at 1050.30 MHz, and the resonance frequency of the cavity is tuned near 1050.40 MHz. (a) Raw noise power spectra when the JPA is on and off. Strong positive peaks are the calibration tone injected at +0.2 MHz, and its image. (b) r and G_J spectra defined in Sec. V in the main text, and the fitted baselines of them drawn with dashed black lines. r is obtained after merging every 5 bins in the JPA on noise power spectrum. (c) The spectrum of r/G_J obtained from the data shown in (b). The solid gray and black dashed lines are obtained using the data and fitted baseline of r divided by the baseline of G_J. (d) Normalized excess of r, calculated using Eq. (10).

procedure outlined at the beginning of this section. Those peaks confirmed to be not due to axion conversion are removed together with their left and right single bins in the vertically combined spectra. For the rest of the candidates, data are taken for at least 3 times longer than the initial acquisition.

The grand spectra from all runs and their rescans are combined once more to report the limit on g_γ. The systematic effect of the baseline estimation is calibrated using a software-synthesized axion signal injected at every 200 kHz in each run. The overall signal detection efficiency is found to fluctuate slightly around 90% in runs 4–6. The effect of the frequency-dependent Gaussian width in run 6 is considered here during the normalization procedure. From this, the final achieved SNR for the axion signals with the DFSZ coupling is calibrated. The combined sensitivity is calculated on the basis of the Bayesian power measurement framework [102]. Figure 21 shows the statistical distribution of the formed excess from the combined runs 5 and 6. About 10% of the candidates above the given threshold are newly found after further improvement of the analysis after rescan, as well as combining runs 4–6. The effect of such candidates on the exclusion of $g_{a\gamma\gamma}$ is naturally reflected by accommodating the Baysian approach. From the achieved SNR, the prior update for the different target SNR and the corresponding coupling strength g_γ at each frequency channel is calculated using the relationship $R_{\text{target}} = g_\gamma^2 R_{\text{achieved}}$, with g_γ normalized to 1 at the DFSZ coupling. Then, the 10% prior update contour with 400 kHz of subaggregate window is set for the frequency-dependent limit corresponding to approximately 90% confidence level at the target SNR of 5σ. The limit from the frequentist threshold (FT) approach is reported as a reference, with the same subaggregate window; see Fig. 22. The exclusion plot shown in Fig. 23 includes all major axion dark-matter experiments and astrophysical limits between approximately 0.5 and 8 GHz. The current work is indicated in the inset. The exclusion plot here corresponds to the blue line of Fig. 22.

VI. DISCUSSION

Over the past few decades, intense experimental effort has been made internationally to probe the vast parameter space for axions and axionlike particles. Cavity-based haloscopes have provided the most sensitive searches in the $\mathcal{O}(10^0)$ GHz range. However, there are only a few attempts to go beyond that, and even then, the sensitivities are still far away from the hadronic axion models. This is mainly due to the loss of cavity detection volume, the

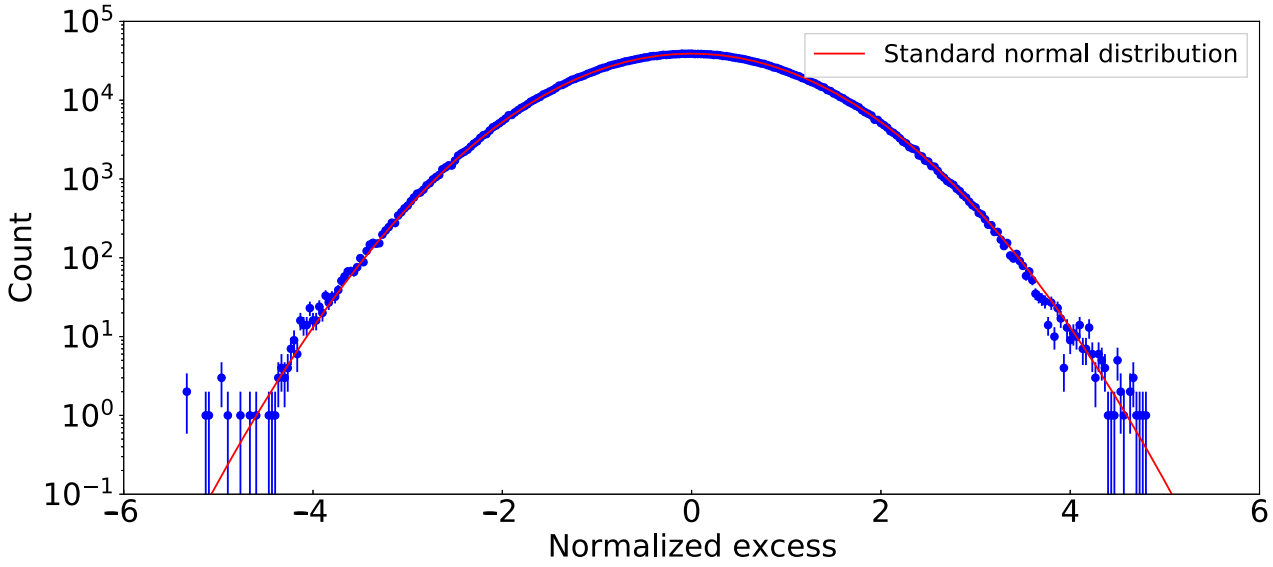

FIG. 21. Statistical distribution of grand spectra excesses for runs 5 and 6. The total number of entries is approximately 3.7×10^6. The negative excesses on the left deviate from the standard normal distribution due to the distortion of the baseline by minor mode crossings.

decrease in the cavity quality factor at higher frequencies, and the linear increase of quantum noise with frequency. Therefore, different approaches are needed to achieve high sensitivity to frequencies higher than 1 GHz.

It was thought for a long time that superconducting cavities would perform worse than copper cavities in a strong magnetic field. Certainly, there have been previous attempts to manufacture superconducting cavities, but they all failed to show any improvement until CAPP's breakthrough achievement using high-temperature superconducting tapes [106–108]. CAPP demonstrated a steady improvement in this field over the years, currently reaching a quality factor of 13×10^6 in 8 T magnetic field. When data acquisition is optimized, the axion scanning rate can be proportional to the cavity quality factor even when it exceeds the axion quality factor [109,110].

CAPP has developed several novel cavity designs that efficiently increase the search frequency, along with practical tuning mechanisms. They include (i) a pizza-cavity design consisting of multiple cells divided by equidistant

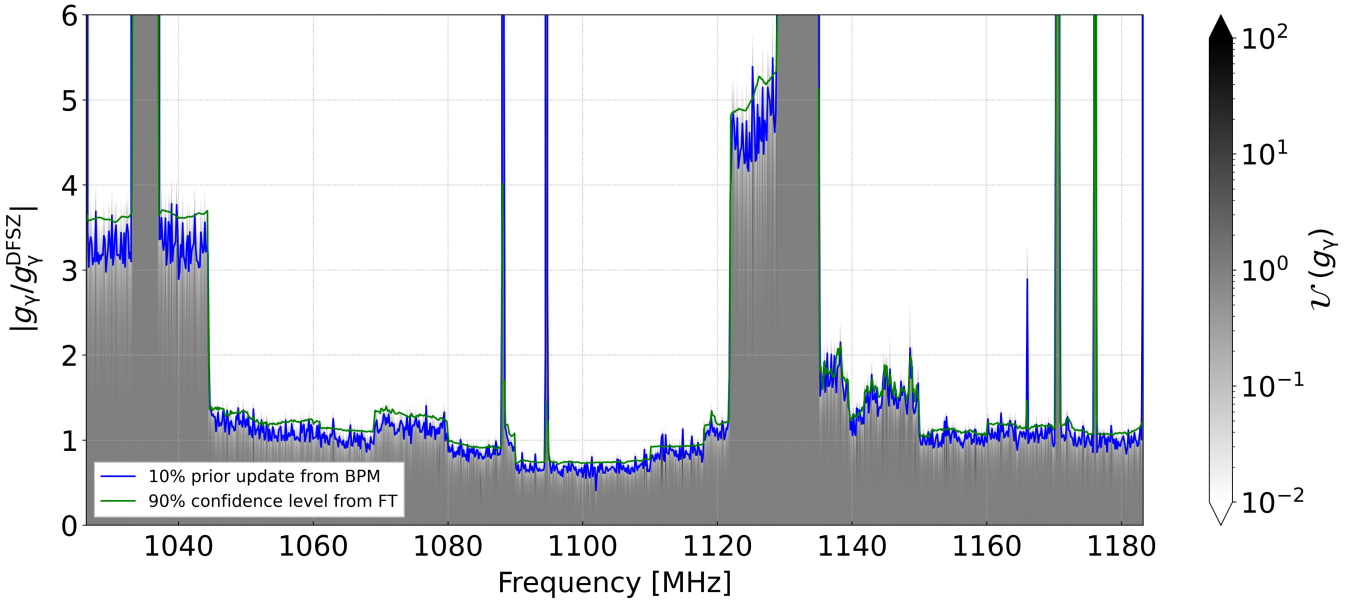

FIG. 22. Exclusion limits for axion-photon coupling obtained using BPM analysis (blue). The 10% prior update contour of the BPM framework is equivalent to the standard 90% exclusion line (green) achieved with the FT framework. The subaggregated prior updates are scaled in gray.

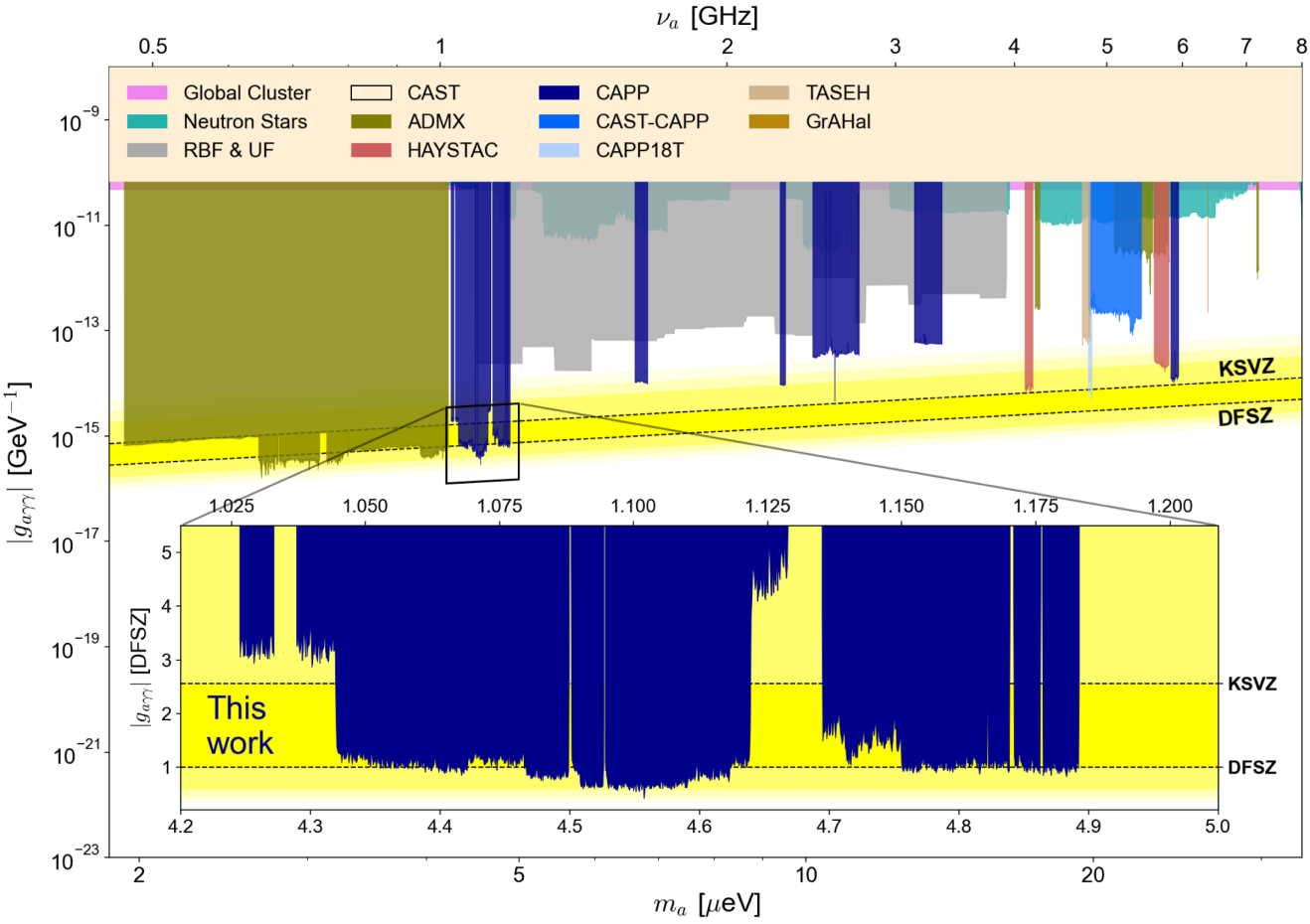

FIG. 23. Exclusion limits set by this work for axion–photon coupling at approximately 90% confidence level assuming that axions are 100% of the local dark-matter density with a value of 0.45 GeV/cm^3. The yellow band represents the areas predicted by the theoretical models of KSVZ and DFSZ. The magnified version is shown in the inset over the mass range between 4.2 and 5.0 μeV. The gaps around 1.0881, 1.0947, 1.1290–1.1350, 1.1705, and 1.1762 GHz correspond to mode crossings. The frequency ranges of 1.0267–1.0443 and 1.1220–1.1229 GHz were scanned with HEMT as the first stage amplifier. The remaining gaps correspond to data whose analysis was not finalized by the publication time for a variety of reasons, including incomplete stored information. The exclusion limits from other experiments (Global Cluster [125], Neutron Stars [126–129], RBF and UF [130,131], CAST [132], ADMX [33–35], HAYSTAC [36–38], CAPP [28–32], CAST-CAPP [48], CAPP18T [133,134], TASEH [135], and GrAHal [136]) are taken from Ref. [137].

partitions [111], tuned by a single carousel-like structure and read out by a single antenna, (ii) a wheel-tuning mechanism suitable for exploiting higher-order resonant modes such as TM_{030} [112], and (iii) a tunable photonic crystal design featuring an array of dielectric rods whose position can be adjusted using an auxetic structure of rotating squares [113]. Our studies indicate that combining these designs can produce microwave resonators suitable for conducting a frequency search spanning three octaves (1–8 GHz) using a cavity structure with a single readout system. They maintain a reasonable geometrical factor within a factor of 2 from the ideal and provide an effective volume of more than 30 l.

In addition, CAPP recently proposed a new search method based on heterodyne interferometry that mixes weak axion-induced photons with strong reference photons [114]. The variance of the interference, whose intensity is proportional to the amplitude of the reference probe, can be measured using a power detector even at high dark count rates, enabling sensitive detection nearly quantum noise limited.

The long-term direction will go toward the development of single-photon detectors, which are overwhelmingly advantageous, particularly at high frequencies and low temperatures. Quantum-limited linear amplifiers are subject to fundamental quantum noise, which is linear in frequency. Single-photon detectors at low temperatures could improve the scanning speed dramatically at high frequencies when their dark count is kept low [115–121] and above 10 GHz [115]. For frequencies below 10 GHz, we are developing axion detection chains based on single-photon counters. The main component of one approach is a chip containing a microwave coplanar waveguide as an input line, terminated by the current-biased Josephson junction used as a photon

switching detector [117]. The second approach involves nanobolometers with a resolution of several zeptojoules [122]. Both approaches, together with the heterodyne interferometry method [114], will significantly increase the scanning speed of the experiment.

In addition, CAPP plans to develop a microwave photon counter based on Rydberg atom quantum technologies [123,124]. The general features of Rydberg atoms, such as large transition dipole moments, energy transition levels in the gigahertz range, tunable transition frequencies via the Stark effect, and long lifetimes on the order of milliseconds, make them suitable for efficient detection of microwave photons.

VII. SUMMARY

We reported on the first high-sensitivity axion haloscope search for frequencies above 1 GHz and a scanned range of more than 150 MHz. The achievement described above was made possible by combining a large aperture 12 T magnet with a 37 l ultralight microwave resonant cavity whose physical temperature was kept between 40 and 22 mK, and JPAs with system noise temperature around 200 mK.

The 12 T magnet consists of two coils, an inner coil based on Nb_3Sn low-temperature superconducting (LTS) cable and an outer coil based on the more conventional NbTi LTS cable, made by Oxford Instruments. The total energy content of the magnet, when fully energized, is 5.562 MJ, comes with a persistent mode switch, and operates reliably within its specifications. We have successfully operated for the first time in the world a large volume, 12 T magnet specifically designed to host cavities in 1–8 GHz, our target frequency range.

The sensitivity of the experiment relies equally well on the ability to thermalize and cool the 37 l microwave cavity and the quantum-noise-limited amplifiers to the lowest possible temperature, preferably below 40 mK. Our ultralight cavity is also implemented for the first time in such large volume successfully without jeopardizing the reliability of its critical parameters in axion dark-matter research. Combined with the state-of-the-art thermalization techniques applied in all the important interfaces we managed to keep the cavity for most of the time well below 40 mK. We gold plated the interfaces when good thermalization was needed and partially or totally isolated the elements when it was appropriate.

The maximum temperature difference between the top and bottom of the cavity was 15 mK, which was slowly reduced as a function of time. Eventually, since this run, we have also improved their thermalization and achieved less than 5 mK temperature difference by using annealed copper tapes between the top and bottom plates of the cavity.

Finally, our JPAs at around 1 GHz are performing near quantum noise limit but with limited bandwidth between 50 and 100 MHz. In order to reduce the need for warm-up and cooldown in the experiment, we have bundled up several JPAs together in an optimum manner in order to maintain most of their performance characteristics without compromising significantly the total system noise.

For all of the above projects we have had a very steep learning curve, and by the time we finished the 150 MHz scan we have learned how to effectively combine all of them with high efficiency. The next project is ready to scan between 1.2 and 1.5 GHz at DFSZ sensitivity at a scan rate of more than 3 MHz per day, with the added benefit of using a tuning rod covered by high-temperature superconducting tape. Superconducting cavities combined with the variance method promise an additional up to 2 orders of magnitude in real calendar scanning efficiency, and it is the main current activity at CAPP.

ACKNOWLEDGMENTS

This work was supported by the Institute for Basic Science (IBS-R017-D1) and JSPS KAKENHI (Grant No. JP22H04937). A. F. v. L. was supported by a JSPS postdoctoral fellowship.

APPENDIX A: BAYESIAN POWER MEASURED ANALYSIS

The exclusion limit on g_γ from the data acquired in all runs and their rescans is evaluated using a Bayesian power measured framework. The posterior probability $P_{\text{posterior}}$ of axion presented at a certain frequency bin is updated by number of observation made by the initial scans and the rescans. For a given observation, the ratio $P_{\text{prior}}/P_{\text{posterior}}$ can be approximated by the Bayes factor of two competing hypotheses (whether or not the signal exists). Then the total update is given by the product of the Bayes factors from all observations at the given frequency. Since the coupling strength g_γ is also unknown, the total update is evaluated until it is meaningful (10^{-2}–10^{2}). The color map in Fig. 22 shows the total update in each frequency bin, aggregated to 300 kHz. The aggregate update can be obtained by the average of the total update in individual bins, by neglecting the frequency dependence of the posterior probability in each aggregate window. The g_γ, which makes the aggregate update to be 0.1, is drawn as blue line in Fig. 22, corresponding to the 90% confidence level on g_γ to be excluded. For comparison, exclusion limit from the threshold-based frequentist approach is also drawn as the green line, aggregated with the same window size.

APPENDIX B: FREQUENCY-DEPENDENT STANDARD DEVIATION AFTER HORIZONTAL COMBINATION AND ITS EFFECT ON THE SNR EFFICIENCY

Figure 25 shows the standard deviation σ_h after the horizontal combination. To examine its frequency dependence, the sample standard deviation is calculated for

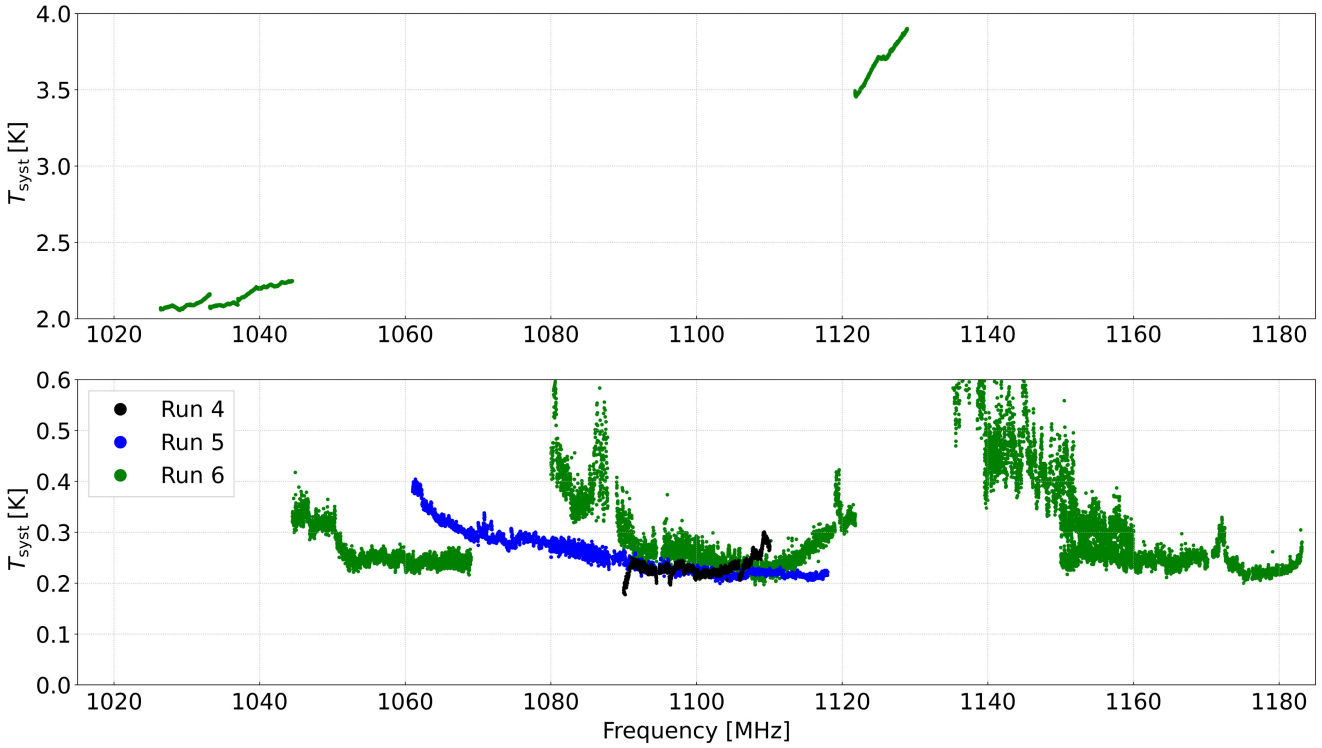

FIG. 24. The system noise temperature T_{syst} throughout runs 4–6. The upper plot shows T_{syst} of the data taken without the JPAs dominated by the HEMT noise, and the lower plot is with the JPAs. Each data point represents T_{syst} of each spectrum, at the resonance frequency of the cavity.

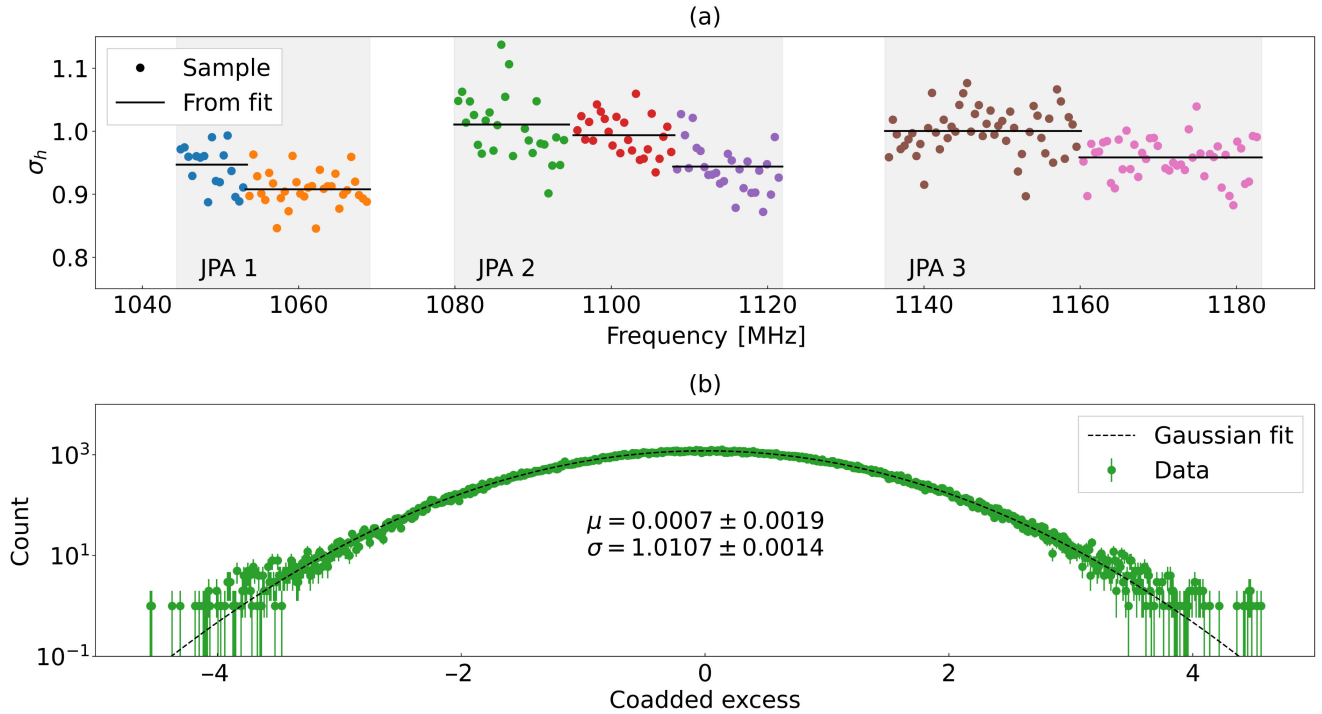

FIG. 25. Standard deviation of the horizontally combined spectra in the region where JPAs are involved in run 6. (a) Sample standard deviation from horizontally combined spectrum. The data points are obtained using 10^4 neighboring channels. Each color represents a distinct data group. The solid horizontal lines indicate a fitted σ from the Gaussian distribution fit of the data groups. (b) Example of the histogram and Gaussian distribution fit. The data belong to the first (1080–1094 MHz) group of JPA 2. The χ^2 goodness of fit is found to be 897.97, with the number of degrees of freedom equal to 897.

every 10^4 neighboring channels. Normally, the horizontally combined spectrum can be normalized once more by σ_h as a frequency-independent normalization factor. However, in run 6, it is not applicable because the resulting distribution will technically be different from a standard normal distribution. To handle the issue, we decided to divide the whole dataset in run 6 into several groups and normalize them separately. The fitted σ_h varies from 0.91 to 1.01 across the groups, which are drawn as black solid lines in Fig. 25. Each group, after the horizontal combination, is normalized by σ_h of their own, then all groups are combined once more vertically to construct the grand spectrum. The distribution of the grand spectrum in runs 5 and 6 combined after this procedure is shown in Fig. 21.

The effect of the frequency-dependent σ_h on the final result is naturally taken into account while estimating the SNR efficiency η_r:

$$\eta_r = \frac{\eta_b}{\sigma_h} \tag{B1}$$

$$= \frac{\eta_b}{\sigma_{h,\mathrm{MC}}}\eta_h. \tag{B2}$$

To estimate η_r, software-synthesized axion signals are added to the data one at a time, with each one at a different frequency. For each injection, the baselines of the power spectra where the signal is injected are estimated once more, and then the rest of the analysis procedures are proceeded. After the horizontal combination, the combined spectrum is subtracted by the original one without the injected signal, in order to reduce the effect of noise. η_b is defined as the ratio between the excess of the signal in this spectrum and the expected SNR of the injected signal when the baseline is perfect. σ_h is involved in estimating η_r while the spectra after the horizontal combination is rescaled to be the standard normal distribution. Thus Eq. (B1) includes the effects from both the imperfect baseline and σ_h.

$\eta_h = \sigma_{h,\mathrm{MC}}/\sigma_h$ is further defined in Eq. (B2), in order to explicitly express the effect of σ_h on η_r. $\sigma_{h,\mathrm{MC}}$ is defined as the standard deviation of the horizontally combined spectrum in the Monte Carlo (MC) simulation. It can be obtained by a psuedo random Gaussian noise on top of the obtained baselines of the noise power spectra. As an example, the first group of JPA 2 (green in Fig. 25) has σ_h of 1.01, and assuming $\sigma_{h,\mathrm{MC}} \sim 0.93$ as previously reported [32], η_h is estimated to be about 0.92. We found η_r to be 0.82 in the first group of JPA 2, 0.90 in run 5 where σ_h was well reproduced by MC simulation, and the ratio of the two being about 0.92 is in a good agreement with the η_h estimated above.

$\sigma_h > \sigma_{h,\mathrm{MC}}$ implies the data in run 6 contain additional sources of statistical error other than the Gaussian fluctuation from the thermal noise. We concluded that the source is the instability of the JPA gain, considering the fact that σ_h is higher in the region where the JPA gain is relatively more unstable. The instability of the JPA gain gets worse in the region where the JPA becomes more sensitive to the external magnetic field, and σ_h reflects this fact as a result. We also confirm that the effect is still observed (with less pronounced) in the analysis using the Savitzky-Golay (SG) filter [100] with a sufficiently narrow window (10 kHz), which means it is not originated from the imperfect baseline model. The model fitting for the baseline is preferred, by considering the combined efficiency η_b in the final analysis result.

APPENDIX C: OPTIMAL COMBINATION OF THE DATA

The signal and idler side of the data are essentially highly correlated, due to the high gain of the JPA and its three-wave-mixing property. That being said, there is still a noticeable statistical improvement possible to be made from the uncorrelated portion of the data as they are combined. To proceed, it is essential to first know the correlation coefficient between the two sides of the data. During the postprocessing of the digitized data, the individual 1920 spectra are not only averaged but also square summed, and furthermore, the product of the two sides is summed. From these statistical measures, the correlation coefficient can be estimated as

$$\rho = \frac{s_{xy}}{s_x s_y}. \tag{C1}$$

s_x is the sample standard deviation defined as

$$s_x = \sqrt{\frac{1}{N-1}\left(\sum_i x_i^2 - N\bar{x}^2\right)}. \tag{C2}$$

$\bar{x} = \sum_i / N$ is the average spectrum for the main analysis, and $\sum_i x_i^2$ is the square sum of the acquired spectra where index i denotes the data in ith spectrum and N is the number of spectra. Similarly,

$$s_{xy} = \frac{1}{N-1}\left(\sum_i x_i y_i - N\bar{x}\,\bar{y}\right). \tag{C3}$$

s_{xy} is the sample covariance, and $\sum_i x_i y_i$ is sum of the signal and idler side product. The subscript y refers to the data at the mirror side, meaning that $y_i(\Delta) = x_i(-\Delta)$, $\bar{y}(\Delta) = \bar{x}(-\Delta)$, and so on, where Δ is the frequency offset from the half pump frequency. The essential term for calculation, namely $\bar{x}$ ($\bar{y}$), $\sum_i x_i^2$ ($\sum_i y_i^2$), and $\sum_i x_i y_i$, are obtained after the time series data are divided and Fourier analyzed. Typical spectra of $\bar{x}$, $s_x s_y$, s_{xy} are shown in Fig. 26. For this figure, the same dataset shown in Fig. 20 is chosen. Overall, the spectra, including ρ, depend greatly on the frequency dependence of the JPA gain, because the JPA is the source of the correlation as it creates the idler copy of any input it receives. The ρ varies depending on the ratio of power between the correlated and uncorrelated portion, and a relatively low ρ

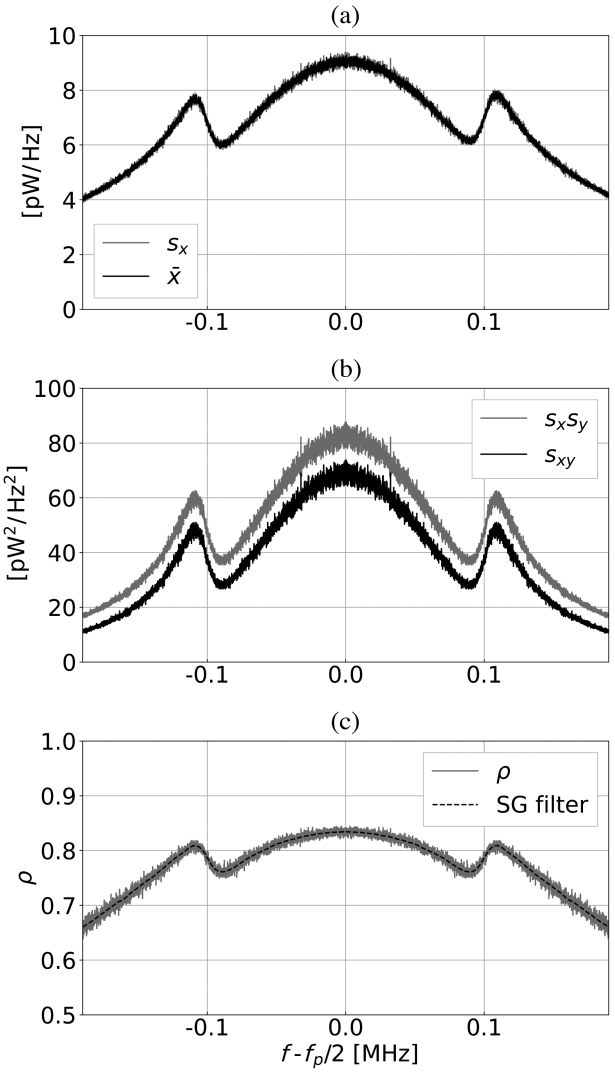

FIG. 26. Spectra used in the correlation analysis. (a) The averaged power spectral density $\bar{x}$, and the standard deviation s_x, (b) the $s_x s_y$ spectrum, the covariance s_{xy}, and (c) the correlation coefficient ρ, all as a function of frequency.

means the improvement from the combination of two sides will be relatively higher.

For the next step, the normalized excess on the two sides is optimally weighted and summed:

$$\delta' = w_s \delta_s + w_I \delta_I, \tag{C4}$$

$$\sigma' = \sqrt{w_s^2 + w_I^2 + 2\rho w_s w_I}. \tag{C5}$$

δ_s (δ_I) is the normalized excess on the signal (idler) side. It follows a Gaussian distribution with a standard deviation of 1, and mean of R_s (R_I) when the axion signal exists. w_s and w_I is the weighting factor for the signal and the idler side. The SNR of combined signal can be expressed as

$$R = \frac{w_s R_s + w_I R_I}{\sqrt{w_s^2 + w_I^2 + 2\rho w_s w_I}}. \tag{C6}$$

The weighting factor w_s and w_I can be optimized in the direction of maximizing R. As a result,

$$w_s = \frac{R_s - \rho R_I}{1-\rho^2}, \qquad w_I = \frac{R_I - \rho R_s}{1-\rho^2} \tag{C7}$$

can be obtained as the optimized weighting factors.

Equation (C6) implies that $w_s' = c w_s$ and $w_I' = c w_I'$ with any arbitrary real number c can also be the optimal weighting factor. As proposed in the HAYSTAC analysis procedure [100], it is convenient to set σ' as the expected SNR of the signal after combining the data. Equations (C7) are chosen such that R and σ' have the same value. Consequently, the combined SNR becomes

$$R = \sigma' = \sqrt{\frac{R_s^2 + R_I^2 - 2\rho R_s R_I}{1-\rho^2}}. \tag{C8}$$

One can find that R is always bigger than both R_s and R_I after optimally combined. For the case of $\rho = 1$, R_s is the same with R_I by definition (two sides are identical), and the combined R simply becomes R_s or R_I. For the case when $R_s \approx R_I$ as the JPA gain is sufficiently large, Eq. (C8) can be approximated as

$$R \approx R_s \sqrt{\frac{2}{1+\rho}}. \tag{C9}$$

For the dataset shown in Fig. 26, the correlation coefficient is found to be ~0.8 on the resonance of the cavity, and it corresponds to ~6% of improvement on the SNR. The maximum improvement of the SNR is found to be ~17% during run 6, where T_{off} was about 3 K.

The normalized excess $\delta = \delta'/\sigma'$ and the combined SNR R can be further combined with the same optimization procedure. Equation (C7) states that $w_s = R_s$ and $w_I = R_I$ for the case of $\rho = 0$. In general, $w_i = R_i$ with $i = 1, \ldots, N$ ($N \geq 2$), and the combined SNR $R = \sqrt{\sum_i R_i^2}$ holds for the independent samples to be combined.

TABLE I. Averaged systematic errors on $g_{a\gamma\gamma}$ and various parameters, assuming no uncertainty on the dark-matter density.

Category	Percentage error
$P_{a\gamma\gamma}$	2.4%
T_{ref}	4.3%
SNRI	1.0%
G_{I}	2.3%
η_r	0.8%
$\text{SNR}_{\text{achieved}}$ (JPA)	5.3%
$g_{a\gamma\gamma}$	2.6%

APPENDIX D: SYSTEMATIC-ERROR ESTIMATION

As previously reported in Ref. [32], the systematic error in $g_{a\gamma\gamma}$ in run 4 is estimated to be about 3% and is similar in run 5 as the system configuration is essentially the same in these runs. It is estimated to be about 8% at maximum in run 6, and the main sources of error are the calibration of the SNR for the idler side signal and the drift of $T_{\rm off}$ due to active devices other than the JPA. The SNR error from the idler side is estimated using the single-tone calibration as described in Sec. V of the main text. This error is frequency dependent and tends to be higher in the region where the JPA performance is not optimal. The drift of $T_{\rm off}$ is the dominant source of systematic error for the data taken without the JPAs in run 6, and its effect on $g_{a\gamma\gamma}$ is around 2%. Consequently, the average systematic error on the combined exclusion limit is approximately 4% at maximum, assuming that there is no correlation between the runs. The systematic errors on $g_{a\gamma\gamma}$ and various parameters are listed in Table I.

[1] C. J. Copi, D. N. Schramm, and M. S. Turner, *Big-bang nucleosynthesis and the baryon density of the universe*, Science **267**, 192 (1995).

[2] N. Aghanim *et al.*, *Planck 2018 results—VI. Cosmological parameters*, Astron. Astrophys. **641**, A6 (2020).

[3] L. Roszkowski, E. M. Sessolo, and S. Trojanowski, *WIMP dark matter candidates and searches—Current status and future prospects*, Rep. Prog. Phys. **81**, 066201 (2018).

[4] M. Schumann, *Direct detection of WIMP dark matter: Concepts and status*, J. Phys. G **46**, 103003 (2019).

[5] F. Chadha-Day, J. Ellis, and D. J. E. Marsh, *Axion dark matter: What is it and why now?*, Sci. Adv. **8**, eabj3618 (2022).

[6] Y. K. Semertzidis and S. Youn, *Axion dark matter: How to see it?*, Sci. Adv. **8**, eabm9928 (2022).

[7] A. M. Green and B. J. Kavanagh, *Primordial black holes as a dark matter candidate*, J. Phys. G **48**, 043001 (2021).

[8] P. Villanueva-Domingo, O. Mena, and S. Palomares-Ruiz, *A brief review on primordial black holes as dark matter*, Front. Astron. Space Sci. **8**, 681084 (2021).

[9] C. Abel *et al.*, *Measurement of the permanent electric dipole moment of the neutron*, Phys. Rev. Lett. **124**, 081803 (2020).

[10] J. Alexander *et al.*, *The storage ring proton EDM experiment*, arXiv:2205.00830.

[11] R. D. Peccei and H. R. Quinn, *CP conservation in the presence of pseudoparticles*, Phys. Rev. Lett. **38**, 1440 (1977).

[12] S. Weinberg, *A new light boson?*, Phys. Rev. Lett. **40**, 223 (1978).

[13] F. Wilczek, *Problem of strong P and T invariance in the presence of instantons*, Phys. Rev. Lett. **40**, 279 (1978).

[14] F. Takahashi, W. Yin, and A. H. Guth, *QCD axion window and low-scale inflation*, Phys. Rev. D **98**, 015042 (2018).

[15] P. W. Graham and A. Scherlis, *Stochastic axion scenario*, Phys. Rev. D **98**, 035017 (2018).

[16] J. Preskill, M. B. Wise, and F. Wilczek, *Cosmology of the invisible axion*, Phys. Lett. B **120**, 127 (1983).

[17] L. F. Abbott and P. Sikivie, *A cosmological bound on the invisible axion*, Phys. Lett. B **120**, 133 (1983).

[18] M. Dine and W. Fischler, *The not-so-harmless axion*, Phys. Lett. B **120**, 137 (1983).

[19] S. Borsanyi *et al.*, *Calculation of the axion mass based on high-temperature lattice quantum chromodynamics*, Nature (London) **539**, 69 (2016).

[20] V. B. Klaer and G. D. Moore, *The dark-matter axion mass*, J. Cosmol. Astropart. Phys. 11 (2017) 049.

[21] M. Buschmann, J. W. Foster, and B. R. Safdi, *Early-universe simulations of the cosmological axion*, Phys. Rev. Lett. **124**, 161103 (2020).

[22] M. S. Turner, *Periodic signatures for the detection of cosmic axions*, Phys. Rev. D **42**, 3572 (1990).

[23] J. E. Kim, *Weak-interaction singlet and strong CP invariance*, Phys. Rev. Lett. **43**, 103 (1979).

[24] M. A. Shifman, A. I. Vainshtein, and V. I. Zakharov, *Can confinement ensure natural CP invariance of strong interactions?*, Nucl. Phys. **B166**, 493 (1980).

[25] A. P. Zhitnitsky, *On possible suppression of axion hadron interactions*, Yad. Fiz. **31**, 497 (1980) [Sov. J. Nucl. Phys. **31**, 260 (1980)].

[26] M. Dine, W. Fischler, and M. Srednicki, *A simple solution to the strong CP problem with a harmless axion*, Phys. Lett. B **104**, 199 (1981).

[27] P. Sikivie, *Experimental tests of the "invisible" axion*, Phys. Rev. Lett. **51**, 1415 (1983).

[28] S. Lee, S. Ahn, J. Choi, B. R. Ko, and Y. K. Semertzidis, *Axion dark matter search around* 6.7 μeV, Phys. Rev. Lett. **124**, 101802 (2020).

[29] J. Jeong, S. W. Youn, S. Bae, J. Kim, T. Seong, J. E. Kim, and Y. K. Semertzidis, *Search for invisible axion dark matter with a multiple-cell haloscope*, Phys. Rev. Lett. **125**, 221302 (2020).

[30] O. Kwon, D. Lee, W. Chung, D. Ahn, H. S. Byun, F. Caspers, H. Choi, J. Choi, Y. Chong, H. Jeong *et al.*, *First results from an axion haloscope at CAPP around* 10.7 μeV, Phys. Rev. Lett. **126**, 191802 (2021).

[31] J. Kim *et al.*, *Near-quantum-noise axion dark matter search at CAPP around* 9.5 μeV, Phys. Rev. Lett. **130**, 091602 (2023).

[32] A. K. Yi, S. Ahn, C. Kutlu, J. M. Kim, B. R. Ko, B. I. Ivanov. H. S. Byun, A. F. van Loo, S. T. Park, J. Jeong *et al.*, *Axion dark matter search around* 4.55 μeV *with Dine-Fischler-Srednicki-Zhitnitskii sensitivity*, Phys. Rev. Lett. **130**, 071002 (2023).

[33] N. Du *et al.* (ADMX Collaboration), *Search for invisible axion dark matter with the axion dark matter experiment*, Phys. Rev. Lett. **120**, 151301 (2018).

[34] T. Braine *et al.* (ADMX Collaboration), *Extended search for the invisible axion with the axion dark matter experiment*, Phys. Rev. Lett. **124**, 101303 (2020).

[35] C. Bartram *et al.* (ADMX Collaboration), *Search for invisible axion dark matter in the* 3.3–4.2 μeV *mass range*, Phys. Rev. Lett. **127**, 261803 (2021).

[36] B. M. Brubaker, L. Zhong, Y. V. Gurevich, S. B. Cahn, S. K. Lamoreaux, M. Simanovskaia, J. R. Root, S. M. Lewis,

S. Al Kenany, K. M. Backes *et al.*, *First results from a microwave cavity axion search at* 24 μeV, Phys. Rev. Lett. **118**, 061302 (2017).
[37] K. Backes *et al.*, *A quantum enhanced search for dark matter axions*, Nature (London) **590**, 238 (2021).
[38] M. J. Jewell *et al.* (HAYSTAC Collaboration), *New results from HAYSTAC's phase II operation with a squeezed state receiver*, Phys. Rev. D **107**, 072007 (2023).
[39] D. Alesini, C. Braggio, G. Carugno, N. Crescini, D. D'Agostino, D. Di Gioacchino, R. Di Vora, P. Falferi, S. Gallo, U. Gambardella *et al.*, *Galactic axions search with a superconducting resonant cavity*, Phys. Rev. D **99**, 101101(R) (2019).
[40] D. Alesini, C. Braggio, G. Carugno, N. Crescini, D. D'Agostino, D. Di Gioacchino, R. Di Vora, P. Falferi, U. Gambardella, C. Gatti *et al.*, *Search for invisible axion dark matter of mass* $m_a = 43$ μeV *with the QUAX–aγ experiment*, Phys. Rev. D **103**, 102004 (2021).
[41] R. Di Vora *et al.* (QUAX Collaboration), *Search for galactic axions with a traveling wave parametric amplifier*, Phys. Rev. D **108**, 062005 (2023).
[42] B. T. McAllister, G. Flower, E. N. Ivanov, M. Goryachev, J. Bourhill, and M. E. Tobar, *The organ experiment: An axion haloscope above 15 GHz*, Phys. Dark Universe **18**, 67 (2017).
[43] A. Quiskamp *et al.*, *Direct search for dark matter axions excluding ALP cogenesis in the* 63- *to* 67-μeV *range with the organ experiment*, Sci. Adv. **8**, 27 (2022).
[44] A. Caldwell, G. Dvali, B. Majorovits, A. Millar, G. Raffelt, J. Redondo, O. Reimann, F. Simon, and F. Steffen, *Dielectric haloscopes: A new way to detect axion dark matter*, Phys. Rev. Lett. **118**, 091801 (2017).
[45] P. Brun *et al.* (MADMAX Collaboration), *A new experimental approach to probe QCD axion dark matter in the mass range above 40 μ*eV, Eur. Phys. J. C **79**, 186 (2019).
[46] S. Knirck *et al.* (MADMAX Collaboration), *Simulating MADMAX in 3D: Requirements for dielectric axion haloscopes*, J. Cosmol. Astropart. Phys. 10 (2021) 034.
[47] L. Brouwer *et al.* (DMRadio Collaboration), *Proposal for a definitive search for GUT-scale QCD axions*, Phys. Rev. D **106**, 112003 (2022).
[48] C. Adair *et al.* (CAST-CAPP Collaboration), *Search for dark matter axions with CAST-CAPP*, Nat. Commun. **13**, 6180 (2022).
[49] D. Alesini *et al.*, *The future search for low-frequency axions and new physics with the FLASH resonant cavity experiment at Frascati National Laboratories*, Phys. Dark Universe **42**, 101370 (2023).
[50] V. Anastassopoulos *et al.* (CAST Collaboration), *New CAST limit on the axion-photon interaction*, Nat. Phys. **13**, 584 (2017).
[51] E. Armengaud *et al.*, *Physics potential of the International Axion Observatory (IAXO)*, J. Cosmol. Astropart. Phys. 06 (2019) 047.
[52] R. Ballou *et al.* (OSQAR Collaboration), *New exclusion limits on scalar and pseudoscalar axionlike particles from light shining through a wall*, Phys. Rev. D **92**, 092002 (2015).
[53] K. Ehret *et al.*, *New ALPS results on hidden-sector lightweights*, Phys. Lett. B **689**, 149 (2010).
[54] R. Baehre *et al.*, *Any light particle search II—Technical design report*, J. Instrum. **8**, T09001 (2013).
[55] D. Kim, J. Jeong, S. Youn, Y. Kim, and Y. K. Semertzidis, *Revisiting the detection rate for axion haloscopes*, J. Cosmol. Astropart. Phys. 03 (2020) 066.
[56] W. Ma *et al.*, *A new member of high field large bore superconducting research magnets family*, IOP Conf. Ser. **502**, 012104 (2019).
[57] Çağlar Kutlu, A. F. van Loo, S. V. Uchaikin, A. N. Matlashov, D. Lee, S. Oh, J. Kim, W. Chung, Y. Nakamura, and Y. K. Semertzidis, *Characterization of a flux-driven Josephson parametric amplifier with near quantum-limited added noise for axion search experiments*, Supercond. Sci. Technol. **34**, 085013 (2021).
[58] A. K. Yi, S. Ahn, C. Kutlu, J. M. Kim, B. R. Ko, B. I. Ivanov. H. S. Byun, A. F. van Loo, S. T. Park, J. Jeong *et al.*, *Search for the Sagittarius tidal stream of axion dark matter around* 4.55 μev, Phys. Rev. D **108**, L021304 (2023).
[59] https://www.oxinst.com.
[60] J. Schleeh, G. Alestig, J. Halonen, A. Malmros, B. Nilsson, P. A. Nilsson, J. P. Starski, N. Wadefalk, H. Zirath, and J. Grahn, *Ultralow-power cryogenic InP HEMT with minimum noise temperature of 1 K at 6 GHz*, IEEE Electron Device Lett. **33**, 664 (2012).
[61] B. I. Ivanov, D. I. Volkhin, I. L. Novikov, D. K. Pitsun, D. O. Moskalev, I. A. Rodionov, E. Il'ichev, and A. G. Vostretsov, *A wideband cryogenic microwave low-noise amplifier*, Beilstein J. Nanotechnol. **11**, 1484 (2020).
[62] https://www.tokyoinst.co.jp/product_file/file/LCG02_xcat01_ja.pdf.
[63] https://fischerconnectors.com/en/circular-connectors/.
[64] https://apiezon.com/products/vacuum-greases/apiezon-n-grease/.
[65] https://bluefors.com/products/liquid-helium-management-products/liquid-helium-plants/.
[66] https://bluefors.com/products/liquid-helium-management-products/helium-reliquefiers/.
[67] COMSOL AB, *COMSOL Multiphysics® v6.0* (COMSOL, Stockholm, Sweden, 2021), https://www.comsol.com/.
[68] Dassault Systèmes, *CST Studio Suite®* (Dassault Systèmes, Vélizy-Villacoublay, France, 2023), https://www.3ds.com/products-services/simulia/products/cst-studio-suite/.
[69] https://www.attocube.com.
[70] N. M. Rapidis, S. M. Lewis, and K. A. van Bibber, *Characterization of the HAYSTAC axion dark matter search cavity using microwave measurement and simulation techniques*, Rev. Sci. Instrum. **90**, 024706 (2019).
[71] J. Ekin, *Experimental Techniques for Low-Temperature Measurements: Cryostat Design, Material Properties and Superconductor Critical-Current Testing* (Oxford University Press, New York, 2006), https://academic.oup.com/book/32506.
[72] L. Zhong, E. P. Menzel, R. D. Candia *et al.*, *Squeezing with a flux-driven Josephson parametric amplifier*, New J. Phys. **15**, 125013 (2013).
[73] A. A. Clerk, M. H. Devoret, S. M. Girvin, F. Marquardt, and R. J. Schoelkopf, *Introduction to quantum noise, measurement, and amplification*, Rev. Mod. Phys. **82**, 1155 (2010).

[74] K. M. Backes, D. A. Palken, S. A. Kenany *et al.*, *A quantum enhanced search for dark matter axions*, Nature (London) **590**, 238 (2021).

[75] T. Yamamoto, K. Inomata, M. Watanabe, K. Matsuba, T. Miyazaki, W. D. Oliver, Y. Nakamura, and J. S. Tsai, *Flux-driven Josephson parametric amplifier*, Appl. Phys. Lett. **93**, 042510 (2008).

[76] A. Roy and M. Devoret, *Introduction to parametric amplification of quantum signals with Josephson circuits*, C.R. Phys. **17**, 740 (2016).

[77] S. V. Uchaikin, B. I. Ivanov, J. Kim *et al.*, *CAPP axion search experiments with quantum noise limited amplifiers*, in *Proceedings of the 29th International Conference on Low Temperature Physics (LT29)* (2023), Vol. 38, p. 011201, 10.7566/JPSCP.38.011201.

[78] ANSYS, Inc., *ANSYS® 2023 R1* (ANSYS, Inc., Canonsburg, PA, USA, 2023).

[79] S. V. Uchaikin, J. Kim, B. I. Ivanov, A. F. van Loo, Y. Nakamura, S. Ahn, S. Oh, S. Park, A. Matlashov, W. Chung, and Y. K. Semertzidis, *Improving amplification bandwidth by combining Josephson parametric amplifiers for active axion search experiments at IBS/CAPP*, J. Low Temp. Phys. **216**, 14 (2024).

[80] S. V. Uchaikin, J. Kim, Çağlar Kutlu, B. I. Ivanov, J. Kim, A. F. v. Loo, Y. Nakamura, S. Ahn, S. Oh, M. Ko, and Y. K. Semertzidis, *Josephson parametric amplifier based quantum noise limited amplifier development for axion search experiments in CAPP*, arXiv:2406.07899.

[81] https://lownoisefactory.com/product/lnf-lnc0-6_2a/.

[82] G. F. Engen, *A new method of characterizing amplifier noise performance*, IEEE Trans. Instrum. Meas. **19**, 344 (1970).

[83] B. I. Ivanov, J. Kim, Ç. Kutlu *et al.*, *Four-channel system for characterization of Josephson parametric amplifiers*, in *Proceedings of the 29th International Conference on Low Temperature Physics (LT29)* (Ref. [77]), p. 011200, 10.7566/JPSCP.38.011200.

[84] J. Kim, M. Ko, S. V. Uchaikin, B. I. Ivanov, A. F. van Loo, Y. Nakamura, S. Oh, V. Gkika, Y. K. Semertzidis, and S. Ahn, *Wideband amplification for IBS-CAPP's axion search experiments*, https://www.researchsquare.com/article/rs-3550142/v1.

[85] P. L. Kapitza, *Heat transfer and superfluidity of helium II*, Phys. Rev. **60**, 354 (1941).

[86] W. A. Little, *The transport of heat between dissimilar solids at low tempeartures*, Can. J. Phys. **37**, 334 (1959).

[87] S. Lee, *Development of a data acquisition software for the CULTASK experiment*, J. Phys. Conf. Ser. **898**, 032035 (2017).

[88] R. Brun and F. Rademakers, *ROOT—An object oriented data analysis framework*, Nucl. Instrum. Methods Phys. Res., Sect. A **389**, 81 (1997).

[89] https://spectrum-instrumentation.com.

[90] S. Ahn, M. J. Lee, A. K. Yi, B. Yeo, B. R. Ko, and Y. K. Semertzidis, *Fast DAQ system with image rejection for axion dark matter searches*, J. Instrum. **17**, P05025 (2022).

[91] F. Caspers (private communication).

[92] M. Vogelsberger and S. D. M. White, *Streams and caustics: The fine-grained structure of Λ cold dark matter haloes*, Mon. Not. R. Astron. Soc. **413**, 1419 (2011).

[93] D. H. H. Hoffmann, J. Jacoby, and K. Zioutas, *Gravitational lensing by the sun of non-relativistic penetrating particles*, Astropart. Phys. **20**, 73 (2003).

[94] B. R. Patla, R. J. Nemiroff, D. H. H. Hoffmann, and K. Zioutas, *Flux enhancement of slow-moving particles by Sun or Jupiter: Can they be detected on Earth?*, Astrophys. J. **780**, 158 (2013).

[95] K. Zioutas *et al.*, *Search for axions in streaming dark matter*, arXiv:1703.01436.

[96] H. Fischer, Y. Semertzidis, and K. Zioutas, *Search for axions in streaming dark matter*, https://ep-news.web.cern.ch/content/search-axions-streaming-dark-matter.

[97] https://www.msit.go.kr/bbs/view.do?bbsSeqNo=83&nttSeqNo=3175660.

[98] S. Ahn, S. Lee, J. Choi, B. R. Ko, and Y. K. Semertzidis, *Improved axion haloscope search analysis*, J. High Energy Phys. 4 (2021) 297.

[99] C. Bartram *et al.* (ADMX Collaboration), *Axion dark matter experiment: Run 1B analysis details*, Phys. Rev. D **103**, 032002 (2021).

[100] B. M. Brubaker, L. Zhong, S. K. Lamoreaux, K. W. Lehnert, and K. A. van Bibber, *HAYSTAC axion search analysis procedure*, Phys. Rev. D **96**, 123008 (2017).

[101] H. Chang *et al.* (TASEH Collaboration), *Taiwan axion search experiment with haloscope: CD102 analysis details*, Phys. Rev. D **106**, 052002 (2022).

[102] D. A. Palken, B. M. Brubaker, M. Malnou, S. A. Kenany, K. M. Backes, S. B. Cahn, Y. V. Gurevich, S. K. Lamoreaux, S. M. Lewis, R. H. Maruyama *et al.*, *Improved analysis framework for axion dark matter searches*, Phys. Rev. D **101**, 123011 (2020).

[103] S. Ahn *et al.* (to be published).

[104] FERRITE-QUASAR, http://ferrite-quasar.ru/aboute.html.

[105] E. J. Daw, *A search for halo axions*, arXiv:1807.09369.

[106] D. Ahn *et al.*, *High quality factor high-temperature superconducting microwave cavity development for the dark matter axion search in a strong magnetic field*, arXiv:1902.04551.

[107] D. Ahn, O. Kwon, W. Chung, W. Jang, D. Lee, J. Lee, S. W. Youn, D. Youm, and Y. K. Semertzidis, *Maintaining high Q-factor of superconducting* $YBa_2Cu_3O_{7-x}$ *microwave cavity in a high magnetic field*, arXiv:1904.05111.

[108] D. Ahn, O. Kwon, W. Chung, W. Jang, D. Lee, J. Lee, S. Woo Youn, H. Byun, D. Youm, and Y. K. Semertzidis, *Biaxially textured* $YBa_2Cu_3O_{7-x}$ *microwave cavity in a high magnetic field for a dark-matter axion search*, Phys. Rev. Appl. **17**, L061005 (2022).

[109] J. Kim, *The first axion quark nugget experiment using a haloscope at CAPP* (private communication), https://agenda.infn.it/event/34455/timetable/#20230706.detailed.

[110] R. Cervantes, G. Carosi, C. Hanretty, S. Kimes, B. H. LaRoque, G. Leum, P. Mohapatra, N. S. Oblath, R. Ottens, Y. Park, G. Rybka, J. Sinnis, and J. Yang, *Search for* 70 μeV *dark photon dark matter with a dielectrically loaded multiwavelength microwave cavity*, Phys. Rev. Lett. **129**, 201301 (2022).

[111] J. Jeong, S. Youn, S. Ahn, J. E. Kim, and Y. K. Semertzidis, *Concept of multiple-cell cavity for axion dark matter search*, Phys. Lett. B **777**, 412 (2018).

[112] J. Kim, S. Youn, J. Jeong, W. Chung, O. Kwon, and Y. K. Semertzidis, *Exploiting higher-order resonant modes for axion haloscopes*, J. Phys. G **47**, 035203 (2020).

[113] S. Bae, S. W. Youn, and J. Jeong, *Tunable photonic crystal haloscope for high-mass axion searches*, Phys. Rev. D **107**, 015012 (2023).

[114] Z. Omarov, J. Jeong, and Y. K. Semertzidis, *Speeding axion haloscope experiments using heterodyne-variance-based detection with a power meter*, Phys. Rev. D **107**, 103005 (2023).

[115] S. K. Lamoreaux, K. A. van Bibber, K. W. Lehnert, and G. Carosi, *Analysis of single-photon and linear amplifier detectors for microwave cavity dark matter axion searches*, Phys. Rev. D **88**, 035020 (2013).

[116] G. Oelsner, C. K. Andersen, M. Rehák, M. Schmelz, S. Anders, M. Grajcar, U. Hübner, K. Mølmer, and E. Il'ichev, *Detection of weak microwave fields with an underdamped Josephson junction*, Phys. Rev. Appl. **7**, 014012 (2017).

[117] L. S. Revin, A. L. Pankratov, A. V. Gordeeva, A. A. Yablokov, I. V. Rakut, V. O. Zbrozhek, and L. S. Kuzmin, *Microwave photon detection by an Al Josephson junction*, Beilstein J. Nanotechnol. **11**, 960 (2020).

[118] A. D'Elia, A. Rettaroli, S. Tocci, D. Babusci, C. Barone, M. Beretta, B. Buonomo, F. Chiarello, N. Chikhi, D. Di Gioacchino *et al.*, *Stepping closer to pulsed single microwave photon detectors for axions search*, IEEE Trans. Appl. Supercond. **33**, 1 (2023), https://ieeexplore.ieee.org/document/9932667.

[119] L. Balembois, J. Travesedo, L. Pallegoix, A. May, E. Billaud, M. Villiers, D. Estève, D. Vion, P. Bertet, and E. Flurin, *Cyclically operated microwave single-photon counter with sensitivity of* 10^{-22} $\mathrm{W}/\sqrt{\mathrm{Hz}}$, Phys. Rev. Appl. **21**, 014043 (2024).

[120] Z. Wang, L. Balembois, M. Rančić, E. Billaud, M. Le Dantec, A. Ferrier, P. Goldner, S. Bertaina, T. Chanelière, D. Esteve, D. Vion, P. Bertet, and E. Flurin, *Single-electron spin resonance detection by microwave photon counting*, Nature (London) **619**, 276 (2023).

[121] C. Braggio, L. Balembois, R. D. Vora, Z. Wang, J. Travesedo, L. Pallegoix, G. Carugno, A. Ortolan, G. Ruoso, U. Gambardella, D. D'Agostino, P. Bertet, and E. Flurin, *Quantum-enhanced sensing of axion dark matter with a transmon-based single microwave photon counter*, arXiv:2403.02321.

[122] J. Govenius, R. E. Lake, K. Y. Tan, and M. Möttönen, *Detection of zeptojoule microwave pulses using electrothermal feedback in proximity-induced Josephson junctions*, Phys. Rev. Lett. **117**, 030802 (2016).

[123] S. Matsuki, I. Ogawa, S. Nakamura, M. Tada, K. Yamamoto, and A. Masaike, *Rydberg-atom cavity detector for dark matter axion search in Kyoto*, Nucl. Phys. B, Proc. Suppl. **51**, 213 (1996).

[124] K. Kim and J. Ahn, *Quantum tomography of Rydberg atom graphs by configurable ancillas*, PRX Quantum **4**, 020316 (2023).

[125] M. J. Dolan, F. J. Hiskens, and R. R. Volkas, *Advancing globular cluster constraints on the axion-photon coupling*, J. Cosmol. Astropart. Phys. 10 (2022) 096.

[126] J. W. Foster, Y. Kahn, O. Macias, Z. Sun, R. P. Eatough, V. I. Kondratiev, W. M. Peters, C. Weniger, and B. R. Safdi, *Green Bank and Effelsberg radio telescope searches for axion dark matter conversion in neutron star magnetospheres*, Phys. Rev. Lett. **125**, 171301 (2020).

[127] J. Darling, *New limits on axionic dark matter from the magnetar PSR J1745-2900*, Astrophys. J. Lett. **900**, L28 (2020).

[128] J. W. Foster, S. J. Witte, M. Lawson, T. Linden, V. Gajjar, C. Weniger, and B. R. Safdi, *Extraterrestrial axion search with the breakthrough listen galactic center survey*, Phys. Rev. Lett. **129**, 251102 (2022).

[129] R. A. Battye, M. J. Keith, J. I. McDonald, S. Srinivasan, B. W. Stappers, and P. Weltevrede, *Searching for time-dependent axion dark matter signals in pulsars*, Phys. Rev. D **108**, 063001 (2023).

[130] S. DePanfilis, A. C. Melissinos, B. E. Moskowitz, J. T. Rogers, Y. K. Semertzidis, W. U. Wuensch, H. J. Halama, A. G. Prodell, W. B. Fowler, and F. A. Nezrick, *Limits on the abundance and coupling of cosmic axions at* $4.5 < m_a < 5.0$ μeV, Phys. Rev. Lett. **59**, 839 (1987).

[131] C. Hagmann, P. Sikivie, N. S. Sullivan, and D. B. Tanner, *Results from a search for cosmic axions*, Phys. Rev. D **42**, 1297(R) (1990).

[132] V. Anastassopoulos, S. Aune, K. Barth *et al.*, *New CAST limit on the axion-photon interaction*, Nat. Phys. **13**, 584 (2017).

[133] B. Yang, H. Yoon, M. Ahn, Y. Lee, and J. Yoo, *Extended axion dark matter search using the CAPP18T haloscope*, Phys. Rev. Lett. **131**, 081801 (2023).

[134] Y. Lee, B. Yang, H. Yoon, M. Ahn, H. Park, B. Min, D. L. Kim, and J. Yoo, *Searching for invisible axion dark matter with an 18 T magnet haloscope*, Phys. Rev. Lett. **128**, 241805 (2022).

[135] H. Chang *et al.* (TASEH Collaboration), *First results from the Taiwan axion search experiment with a haloscope at* 19.6 μeV, Phys. Rev. Lett. **129**, 111802 (2022).

[136] T. Grenet, R. Ballou, Q. Basto *et al.*, *The Grenoble axion haloscope platform (GrAHal): Development plan and first results*, arXiv:2110.14406.

[137] C. O'Hare, *cajohare/axionlimits: Axionlimits*, https://cajohare.github.io/AxionLimits/.